Characterization of Errors in Satellite-based HCHO/NO₂ Tropospheric Column Ratios with Respect to Chemistry, Column to PBL Translation, Spatial Representation, and Retrieval Uncertainties

Amir H. Souri[1]*, Matthew S. Johnson[2], Glenn M. Wolfe[3], James H. Crawford[4], Alan Fried[5], Armin Wisthaler[6,7], William H. Brune[8], Donald R. Blake[9], Andrew J. Weinheimer[10], Tijl Verhoelst[11], Steven Compernolle[11], Gaia Pinardi[11], Corinne Vigouroux[11], Bavo Langerock[11], Sungyeon Choi[3,12], Lok Lamsal[3,13], Lei Zhu[14,15], Shuai Sun[14,15], Ronald C. Cohen[16,17], Kyung-Eun Min[18], Changmin Cho[18], Sajeev Philip[19], Xiong Liu[1], and Kelly Chance[1]

[1]Atomic and Molecular Physics (AMP) Division, Center for Astrophysics | Harvard & Smithsonian, Cambridge, MA, USA
[2]Earth Science Division, NASA Ames Research Center, Moffett Field, CA, USA
[3]NASA Goddard Space Flight Center, Greenbelt, MD, USA
[4]NASA Langley Research Center, Hampton, VA, USA
[5]Institute of Arctic & Alpine Research, University of Colorado, Boulder, CO, USA
[6]Institute for Ion Physics and Applied Physics, University of Innsbruck, Technikerstrasse 25, 6020 Innsbruck, Austria
[7]Department of Chemistry, University of Oslo, P.O. box 1033, Blindern, 0315 Oslo, Norway
[8]Department of Meteorology and Atmospheric Science, Pennsylvania State University, University Park, PA, USA
[9]Department of Chemistry, University of California, Irvine, CA, USA
[10]National Center for Atmospheric Research, Boulder, CO, USA
[11]Royal Belgian Institute for Space Aeronomy (BIRA-IASB), Ringlaan 3, 1180 Uccle, Belgium
[12]Science Systems and Applications, Inc., Lanham, MD 20706, USA
[13]Universities Space Research Association, Columbia, MD 21046, USA
[14]School of Environmental Science and Engineering, Southern University of Science and Technology, Shenzhen, Guangdong, China
[15]Guangdong Provincial Observation and Research Station for Coastal Atmosphere and Climate of the Greater Bay Area, Shenzhen, Guangdong, China
[16]Department of Earth and Planetary Science, University of California Berkeley, Berkeley, CA 94720, USA
[17]Department of Chemistry, University of California Berkeley, Berkeley, CA 94720, USA
[18]School of Earth Sciences and Environmental Engineering, Gwangju Institute of Science and Technology, Gwangju, South Korea
[19]Centre for Atmospheric Sciences, Indian Institute of Technology Delhi, New Delhi, India

* Corresponding Author: ahsouri@cfa.harvard.edu

Abstract.

The availability of formaldehyde (HCHO) (a proxy for volatile organic compound reactivity) and nitrogen dioxide (NO₂) (a proxy for nitrogen oxides) tropospheric columns from Ultraviolet-Visible (UV-Vis) satellites has motivated many to use their ratios to gain some insights into the near-surface ozone sensitivity. Strong emphasis has been placed on the challenges that come with transforming what is being observed in the tropospheric column to what is actually in the planetary boundary layer (PBL) and near the surface; however, little attention has been paid to

48   other sources of error such as chemistry, spatial representation, and retrieval uncertainties. Here
49   we leverage a wide spectrum of tools and data to quantify those errors carefully.

50   Concerning the chemistry error, a well-characterized box model constrained by more than
51   500 hours of aircraft data from NASA's air quality campaigns is used to simulate the ratio of the
52   chemical loss of HO_2+RO_2 (LROx) to the chemical loss of NO_x (LNOx). Subsequently, we
53   challenge the predictive power of $HCHO/NO_2$ ratios (FNRs), which are commonly applied in
54   current research, at detecting the underlying ozone regimes by comparing them to LROx/LNOx.
55   FNRs show a strongly linear (R^2=0.94) relationship to LROx/LNOx, but only in the logarithmic
56   scale. Following the baseline (i.e., ln(LROx/LNOx) = -1.0±0.2) with the model and mechanism
57   (CB06, r2) used for segregating NOx-sensitive from VOC-sensitive regimes, we observe a broad
58   range of FNR thresholds ranging from 1 to 4. The transitioning ratios strictly follow a Gaussian
59   distribution with a mean and standard deviation of 1.8 and 0.4, respectively. This implies that FNR
60   has an inherent 20% standard error (1-sigma) resulting from not accurately describing the ROx-
61   HOx cycle. We calculate high ozone production rates (PO_3) dominated by large $HCHO \times NO_2$
62   concentration levels, a new proxy for the abundance of ozone precursors. The relationship between
63   PO_3 and $HCHO \times NO_2$ becomes more pronounced when moving towards NOx-sensitive regions
64   due to non-linear chemistry; our results indicate that there is fruitful information in the
65     $HCHO \times NO_2$ metric that has not been utilized in ozone studies. The vast amount of vertical
66   information on HCHO and NO_2 concentration from the air quality campaigns enables us to
67   parameterize the vertical shapes of FNRs using a second-order rational function permitting an
68   analytical solution for an altitude adjustment factor to partition the tropospheric columns to the
69   PBL region. We propose a mathematical solution to the spatial representation error based on
70   modeling isotropic semivariograms. Based on summertime averaged data, Ozone Monitoring
71   Instrument (OMI) loses 12% of spatial information at its native resolution with respect to a high-
72   resolution sensor like TROPOspheric Monitoring Instrument (TROPOMI) ($>5.5 \times 3.5$ km^2). A
73   pixel with a grid size of 216 km^2 fails at capturing ~65% of the spatial information in FNRs at a
74   50 km length scale comparable to the size of a large urban center (e.g., Los Angeles). We
75   ultimately leverage a large suite of in-situ and ground-based remote sensing measurements to draw
76   the error distributions of daily TROPOMI and OMI tropospheric NO_2 and HCHO columns. At a
77   68% confidence interval (1 sigma), errors pertaining to daily TROPOMI observations, either
78   HCHO or tropospheric NO_2 columns, should be above $1.2\text{-}1.5 \times 10^{16}$ molec.cm^{-2} to attain 20-30%
79   standard error in the ratio. This level of error is almost non-achievable with OMI, given its large
80   error in HCHO.

81   The satellite column retrieval error is the largest contributor to the total error (40-90%) in
82   the FNRs. Due to a stronger signal in cities, the total relative error (<50%) tends to be mild,
83   whereas areas with low vegetation and anthropogenic sources (e.g., Rocky Mountains) are
84   markedly uncertain (>100%). Our study suggests that continuing development in the retrieval
85   algorithm and sensor design and calibration is essential to be able to advance the application of
86   FNRs beyond a qualitative metric.

1. Introduction

88   Accurately representing the near-surface ozone (O_3) sensitivity to its two major precursors,
89   nitrogen oxides (NOx) and volatile organic compounds (VOCs), is an imperative step in
90   understanding non-linear chemistry associated with ozone production rates in the atmosphere.
91   While it is often tempting to characterize an airshed as NOx or VOC-sensitive, both conditions are
92   expected as VOC-sensitive (ozone production rates sensitive to VOC) conditions near NOx
93   sources transition to NOx-sensitive (ozone production rates sensitive to NOx) conditions

94 downwind as NOx dilutes. Thus, reducing the footprint of ozone production can mostly be
95 achieved through NOx reductions. VOCs are key to determining both the location and peak in
96 ozone production, which varies nonlinearly to the NOx abundance. Thus, knowledge of the relative
97 levels of NOx and VOCs informs the trajectory of ozone production and expectations of where
98 peak ozone will occur as emissions change. While a large number of surface stations regularly
99 monitor the near-surface ambient nitrogen dioxide (NO_2) concentrations, the measurements of
100 several VOCs with different reactivity rates with respect to hydroxyl (OH) are not routinely
101 available. As such, our knowledge of where and when ozone production rates are elevated, and
102 their quantitative dependence on a long list of ozone precursors, is fairly limited, except for
103 observationally-rich air quality campaigns. This limitation has prompted several studies, such as
104 Sillman et al. (1990), Tonnesen and Dennis (2000a,b), and Sillman and He (2002), to investigate
105 if the ratio of certain measurable compounds can diagnose ozone regimes meaning if the ozone
106 production rate is sensitive to NOx (i.e., NOx-sensitive) or VOC (i.e., VOC-sensitive). Sillman
107 and He (2002) suggested that H_2O_2/HNO_3 was a robust, measurable ozone indicator as this ratio
108 could well describe the chemical loss of HO_2+RO_2 (LROx) to the chemical loss of NOx (LNOx)
109 controlling the O_3-NOx-VOC chemistry (Kleinman et al., 2001). Nonetheless, both H_2O_2 and
110 HNO_3 measurements are limited to a few spatially-sparse air quality campaigns.
111   Formaldehyde (HCHO) is an oxidation product of VOCs, and its relatively short lifetime
112 (~1-9 hr) makes the location of its primary and secondary sources rather identifiable (Seinfield and
113 Pandis, 2006; Fried et al., 2020). Fortunately, monitoring HCHO abundance in the atmosphere has
114 been a key goal of many Ultraviolet-Visible (UV-Vis) viewing satellites for decades (Chance et
115 al., 1991; Chance et al., 1997; Chance et al., 2000; González Abad et al., 2015; De Smedt et al.,
116 2008, 2012, 2015, 2018, 2021) with reasonable spatial coverage. Additionally, the strong
117 absorption of NO_2 in the UV-Vis range has permitted measurements of NO_2 columns from space
118 (Martin et al., 2002; Boersma et al., 2004, 2007, 2018).
119   Advancements in satellite remote-sensing of these two key compounds have encouraged
120 many studies to elucidate if the ratio of $HCHO/NO_2$ (hereafter FNR) could be a robust ozone
121 indicator (Tonnensen and Dennis, 2000b; Martin et al., 2004; Duncan et al., 2010). Most studies
122 using the satellite-based FNR columns attempted to provide a qualitative view of the underlying
123 chemical regimes (e.g., Choi et al., 2012; Choi and Souri, 2015a,b; Jin and Holloway, 2015; Souri
124 et al., 2017; Jeon et al., 2018; Lee et al., 2021). Relatively few studies (Duncan et al., 2010; Jin et
125 al., 2017; Schroeder et al., 2017; Souri et al., 2020) have carefully tried to provide a quantitative
126 view of the usefulness of the ratio. For the most part, the inhomogeneous vertical distribution of
127 FNR in columns has been emphasized. Jin et al. (2017) and Schroeder et al. (2017) showed that
128 differing vertical shapes of HCHO and NO_2 can cause the vertical shape of FNR not to be
129 consistent throughout the troposphere leading to a variable relationship between what is being
130 observed from the satellite and what is actually occurring in the lower atmosphere. Jin et al. (2017)
131 calculated an adjustment factor to translate the column to the surface using a relatively coarse
132 global chemical transport model. The adjustment factor showed a clear seasonal cycle stemming
133 from spatial and temporal variability associated with the vertical sources and sinks of HCHO and
134 NO_2, in addition to the atmospheric dynamics. In a more data-driven approach, Schroeder et al.
135 (2017) found that the detailed differences in the boundary layer vertical distributions of HCHO
136 and NO_2 lead to a wide range of ambiguous ratios. Additionally, ratios were shown to shift on high
137 ozone days, raising questions regarding the value of satellite averages over longer timescales. Our
138 research aims to put together an integrated and data-driven mathematical formula to translate the

139 tropospheric column to the planetary boundary layer (PBL), exploiting the abundant aircraft
140 measurements available during ozone seasons.
141   Using observationally-constrained box models, Souri et al. (2020) demonstrated that there
142 was a fundamentally inherent uncertainty related to the ratio originating from the chemical
143 dependency of HCHO on NO_x (Wolfe et al., 2016). In VOC-rich (poor) environments, the
144 transitioning ratios from NOx-sensitive to VOC-sensitive occurred in larger (smaller) values than
145 the conventional thresholds defined in Duncan et al. (2010) due to an increased (dampened) HCHO
146 production induced by NOx. To account for the chemical feedback and to prevent a wide range of
147 thresholds on segregating NOx-sensitive from VOC-sensitive regions, Souri et al. (2020)
148 suggested using a first-order polynomial matched to the ridgeline in $P(O_3)$ isopleths. Their study
149 illuminated the fact that the ratio suffers from an inherit chemical complication. However, Souri
150 et al. (2020) did not quantify the error, and their work was limited to a subset of atmospheric
151 conditions. To challenge the predictive power of FNR from a chemistry perspective, we will take
152 advantage of a large suite of datasets to make maximum use of varying meteorological and
153 chemical conditions.
154   Not only are satellite-based column measurements unable to resolve the vertical
155 information of chemical species in the tropospheric column, but they are also unable to resolve the
156 horizontal spatial variability due to their spatial footprint. The larger the footprint is, the more
157 horizontal information is blurred out. For instance, Souri et al. (2020) observed a substantial spatial
158 variance (information) in FNR columns at the spatial resolution of 250×250 m^2 observed by an
159 airborne sensor over Seoul, South Korea. It is intuitively clear that a coarse-resolution sensor
160 would lose a large degree of spatial variance (information). This error, known as the spatial
161 representation error, has not been studied with respect to FNR. We will leverage what we have
162 learned from Souri et al. (2022), which modeled the spatial heterogeneity in discrete data using
163 geostatistics, to quantify the spatial representation error in the ratio over an urban environment.
164   A longstanding challenge is to have a reliable estimate of the satellite retrieval errors of
165 tropospheric column NO_2 and HCHO. Significant efforts have been made recently to assemble,
166 analyze, and estimate the retrieval errors for two key satellite sensors, TROPOspheric Monitoring
167 Instrument (TROPOMI) and Ozone Monitoring Instrument (OMI), using various in-situ
168 measurements (Verhoelst et al., 2021; Vigouroux et al., 2020, Choi et al., 2020; Laughner et al.,
169 2019; Zhu et al., 2020). This study will exploit paired comparisons from some of these new studies
170 to propagate individual uncertainties in HCHO and NO_2 to the FNR errors.
171   The overarching science goal of this study is to address the fact that the accurate diagnosis
172 of surface O_3 photochemical regimes is impeded by numerous uncertainty components, which will
173 be addressed in the current paper, and can be classified into four major categories: i) inherent
174 uncertainties associated with the approach of FNRs to diagnose local O_3 production and sensitivity
175 regimes, ii) translation of tropospheric column satellite retrievals to represent PBL- or surface-
176 level chemistry, iii) spatial representativity of ground pixels of satellite sensors, and iv)
177 uncertainties associated with satellite-retrieved column-integrated concentrations of HCHO and
178 NO_2. We will address all of these sources of uncertainty using a broad spectrum of data and tools.
179   Our paper is organized into the following sections. Section 2 describes the chemical box
180 model setup and data applied. Sections 3.1 to 3.4 deal with the chemistry aspects of FNRs and
181 show the results from a box model. Section 3.5 introduces a data-driven framework to transform
182 the FNR tropospheric columns to the PBL region. Section 3.6 offers a new way to quantify the
183 spatial representation error in satellites. Section 3.7 deals with the satellite error characterization

4

184 and its impacts on the ratio. Section 3.8 summarizes the fractional contribution of each error to the
185 combined error. Finally, Section 4 provides a summary and conclusions of the study.

2. Photochemical Box Modeling and Aircraft Data Used

187   To quantify the uncertainty of FNR from a chemistry perspective and to obtain several
188 imperative parameters, including the calculated ozone production rates and the loss of NO_x (LNO_x)
189 and RO_x (LRO_x), we utilize the Framework for 0-D Atmospheric Modeling (F0AM) v4 (Wolfe et
190 al., 2016). We adopt the Carbon Bond 6 (CB06, r2) chemical mechanism, and heterogenous
191 chemistry is not considered in our simulations. The model is initialized with the measurements of
192 several compounds, many of which constrain the model by being held constant for each timestep
193 (see Table 1).
194   Figure 1 shows the map of data points from Deriving Information on Surface Conditions
195 from Column and Vertically Resolved Observations Relevant to Air Quality (DISCOVER-AQ)
196 Baltimore-Washington (2011), DISCOVER-AQ Houston-Texas (2013), DISCOVER-AQ
197 Colorado (2014), and Korea United States Air Quality Study (KORUS-AQ) (2016).
198 Meteorological inputs come from the observed pressure, temperature, and relative humidity. The
199 measurements of photolysis rates are not available for all photolysis reactions; therefore, our initial
200 guess of those rates comes from a look-up-table populated by the National Center for Atmospheric
201 Research (NCAR) Tropospheric Ultraviolet And Visible (TUV) model calculations. These values
202 are a function of solar zenith angle, total ozone column density, surface albedo, and altitude. We
203 set the total ozone column and the surface albedo to fixed numbers of 325 (Dobson) DU and 0.15,
204 respectively. The initial guess is then corrected by applying the ratio of observed photolysis rates
205 of NO_2+hv (jNO_2) and/or O_3+hv (jO^1D) to the calculated ones to all j-values (i.e., wavelength-
206 independent). If both observations of jNO_2 and jO^1D are available, the correction factor is
207 averaged. The KORUS-AQ campaign is the only one that provides jO^1D measurements; therefore,
208 the use of the wavelength-independent correction factor based on the ratio of observed to
209 calculated jNO_2 values for all j-value is a potential source of error in the model especially when
210 aerosols are present. The model calculations are based on the observations merged to a temporal
211 resolution varying from 10 to 15 seconds. Each calculation was run for five consecutive days with
212 an integration time of 1 hour to approach diel steady state. We test the number of solar cycles
213 against ten days on the KORUS-AQ setup and observe no noticeable difference in simulated OH
214 and HCHO (Figure S1), indicating that five solar cycles suffice. Some secondarily-formed species
215 must be unconstrained for the purpose of model validation. Therefore, the concentrations of several
216 secondarily-formed compounds, such as HCHO and PAN, are unconstrained. Nitric oxide (NO)
217 and NO_2 are also allowed to cycle while their sum (i.e., NOx) is constrained. Because the model
218 does not consider various physical loss pathways, including deposition and transport, which vary
219 by time and space, we oversimplify their physical loss through a first-order dilution rate set to
220 $1/86400 - 1/43200$ s^{-1} (i.e., 24- or 12-hr lifetime), which in turn prevents relatively long-lived
221 species from accumulating over time. Our decision on unconstraining HCHO, a pivotal compound
222 impacting the simulation of HOx, may introduce some systematic biases in the simulation of
223 radicals determining ozone chemistry (Schroeder et al., 2020). Therefore, to mitigate the potential
224 bias in HCHO, we set the dilution factor to maintain the campaign-averaged bias in the simulated
225 HCHO with respect to observations of less than 5%. However, it is essential to recognize that
226 HCHO can fluctuate freely for each point measurement because the dilution constraint is set to a
227 fixed value for an individual campaign. Each time tag is independently simulated, meaning we do
228 not initialize the next run using the simulated values from the previous one; this in turn, permits
229 parallel computation. Regarding the KORUS-AQ campaign where HOx observations were

230 available, we only ran the model for data points with HOx measurements. Similar to Souri et al.
231 (2020), we filled gaps in VOC observations with a bilinear interpolation method with no
232 extrapolation allowed. In complex polluted atmospheric conditions such as that over Seoul, South
233 Korea, Souri et al. (2020) observed that this simple treatment yielded comparable results with
234 respect to the NASA LaRC model (Schroeder et al. 2020), which incorporated a more
235 comprehensive data harmonization. Table 1 lists the major configuration along with the
236 observations used for the box model.

237   Several parameters are calculated based on the box model outputs. LRO_x is defined through
238 the sum of primarily radical-radical reactions:

$$LRO_x = k_{HO_2+HO_2}[HO_2]^2 + \sum k_{RO_{2i}+HO_2}[RO_{2i}][HO_2]$$
$$+ \sum k_{RO_{2i}+RO_{2i}}[RO_{2i}]^2 \tag{1}$$

239 where k is the reaction rate constant. LNO_x mainly occurs via the NO_2+OH reaction:

$$LNO_x = k_{OH+NO_2+M}[OH][NO_2][M] \tag{2}$$

240 where M is a third body. We calculate $P(O_3)$ by subtracting the ozone loss pathways dictated by
241 HO_x ($HO+HO_2$), NO_2+OH, O_3 photolysis, ozonolysis, and the reaction of $O(^1D)$ with water vapor
242 from the formation pathways through the removal of NO via HO_2 and RO_2:

$$P(O_3) = k_{HO_2+NO}[HO_2][NO] + \sum k_{RO_{2i}+NO}[RO_{2i}][NO]$$
$$- k_{OH+NO_2+M}[OH][NO_2][M] - P(RONO_2) - k_{HO_2+O_3}[HO_2][O_3]$$
$$- k_{OH+O_3}[OH][O_3] - k_{O(^1D)+H_2O}[O(^1D)][H_2O] - L(O_3$$
$$+ alkenes) \tag{3}$$

3. Results and Discussion

3.1. *Box Model Validation*

245   There are uncertainties associated with the box model (e.g., Brune et al., 2022; Zhang et
246 al., 2021; Lee et al., 2021), which can be attributed to: i) the lack of inclusion of physical processes
247 such as entrainment/detrainment and diffusion, ii) discounting the heterogeneous chemistry, iii)
248 invalid assumption of the diel steady state in areas close to large emission sources or in
249 photochemically less active environments (Thornton et al., 2002; Souri et al., 2021), iv) errors in
250 the chemical mechanism and v) errors in the measurements. These limitations necessitate a
251 thorough validation of the model using unconstrained observations. While models have been
252 known for a long time not to be 100% accurate (Box, 1976), it is important to characterize whether
253 the model can effectively represent reality. For instance, if the simulated HCHO is poorly
254 correlated with observations and/or displayed large magnitude biases, it will be erroneous to
255 assume that the sources of HCHO, along with relevant chemical pathways, are appropriate. It is
256 important to acknowledge that the VOC constraints for these model calculations are incomplete,
257 especially for the DISCOVER-AQ campaigns, which lacked comprehensive VOC observations.
258 Nevertheless, we will show that the selected VOCs are sufficient to reproduce a large variance
259 (>70%) in observed HCHO.

260   We diagnose the performance of the box model by comparing the simulated values of five
261 compounds to observations: HCHO, NO, NO_2, PAN, hydroperoxyl radical (HO_2), and OH. Figure
262 2 depicts the scatterplot of the comparisons along with several statistics. HCHO observations are
263 usually constrained in box models to improve the representation of HO_2 (Schroeder et al., 2017;

264   Souri et al., 2020; Brune et al., 2022); however, this constraint may mask the realistic
265   characterization of the chemical mechanism with respect to the treatment of VOCs. Additionally,
266   it is important to know if the sources of HCHO are adequate. Therefore, we detach the model from
267   this constraint to perform a more fair and stringent validation.
268   Concerning HCHO, our model does have considerable skill at reproducing the variability
269   of observed HCHO (R^2=0.73). To evaluate if this agreement is accidentally caused by the choice
270   of the dilution factor and to identify if our VOC treatment is inferior compared to the one adopted
271   in the NASA LaRC (Schroeder et al., 2021), we conducted three sets of sensitivity tests for the
272   KORUS-AQ campaign, including ones with and without considering a dilution factor and another
273   one without HNO_3 and H_2O_2 constraints (Figure S2). The lack of consideration of a dilution factor
274   results in no difference in the variance in HCHO captured by our model (R^2=0.81). Our model
275   without the dilution factor is still skillful at replicating the magnitude of HCHO with less than 12%
276   bias. This is why the optimal dilution factor for each campaign is within 12 hr to 24 hr, which is
277   not different from other box modeling studies (e.g., Brune et al., 2022; Miller and Brune, 2022).
278   We observe no difference in the simulated HCHO when HNO_3 and H_2O_2 values are not
279   constrained. The unconstrained NASA LaRC setup oversampled at 10-sec frequency captures 86%
280   variance in the measurements, only slightly (6%) outperforming our result. However, the
281   unconstrained NASA LaRC setup greatly underestimates the magnitude of HCHO compared to
282   our model results.
283   The model performs well with regard to the simulation of NO (R^2=0.89) and NO_2 (R^2=0.99)
284   in the logarithmic scale. Immediately evident is the underestimation of NO in highly polluted
285   regions, contrary to an overestimation in clean ones. This discrepancy leads to an underestimation
286   (overestimation) of NO/NO_2 in polluted (clean) regions. The primary drivers of NO/NO_2 are jNO_2
287   and O_3, both of which are constrained in the model. What can essentially deviate the partitioning
288   between NO and NO_2 from that of observations in polluted areas is the assumption of the diel
289   steady state, which is rarely strictly valid where measurements are close to large emitters. The
290   overestimation of NO in low NO_x areas is often blamed on the lack of chemical sink pathways of
291   NO in chemical mechanisms (e.g., Newland et al., 2021). The relatively reasonable performance
292   of PAN (R^2=0.63) is possibly due to constraining some of the oxygenated VOCs, such as
293   acetaldehyde. Xu et al. (2021) observed a strong dependency of PAN concentrations on NO/NO_2
294   ratios. Smaller NO/NO_2 ratios are usually associated with larger PAN mixing ratios because NO
295   can effectively remove peroxyacetyl radicals. We observe an overestimated PAN (0.27 ppbv),
296   possibly due to an underestimation of NO/NO_2. Moreover, we should not rule out the impact of
297   the first-order dilution factor, which was only empirically set in this study. For instance, if we
298   ignore the dilution process for the KORUS-AQ campaign, the bias of the model in terms of PAN
299   will increase by 33% resulting in poor performance (R^2=0.40) (Figure S3). We notice that this
300   poor performance primarily occurs for high altitude measurements where PAN is thermally stable
301   (Figure S4); therefore, this does not impact the majority of rapid atmospheric chemistry occurring
302   in the lower troposphere, such as the formation of HCHO. Schroeder et al. (2020) found that proper
303   simulation of PAN in the polluted PBL during KORUS-AQ required a first-order loss rate based
304   on thermal decomposition at the average PBL temperature, which was more realistic than the
305   widely varying local PAN lifetimes associated with temperature gradients between the surface and
306   the top of the PBL. This solution is computationally equivalent to the dilution rate used in this
307   study.
308   KORUS-AQ was the only field campaign providing OH and HO_2 measurements.
309   Concerning HO_2, former studies such as Schroeder et al. (2017), Souri et al. (2020), and Brune et

310   al. (2022) managed to reproduce HO_2 mixing ratios with R^2 ranging from 0.6 to 0.7. The
311   performance of our model (R^2=0.66) is similar to these past studies, with nearly negligible biases
312   (<1%). One may argue that the absence of the HO_2 uptake by aerosols is contributing to some of
313   the discrepancies we observe in the HO_2 comparison. Brune et al. (2022) provided compelling
314   evidence showing that considering the HO_2 uptake made their results significantly inconsistent
315   with the observations suggesting that the HO_2 uptake might have been inconsequential during the
316   campaign. Our model manages to reproduce 64% of the variance of observed OH outperforming
317   the simulations presented in Souri et al. (2020) and Brune et al. (2022) by >10%. The slope (=
318   1.03) is not too far from the identity line, indicating that our box model systematically
319   overestimates OH by $0.62 \ 10^6$ cm^{-3}. This may be attributed to a missing OH sink in the mechanism
320   or the lack of inclusion of some VOCs. A sensitivity test involving removing the first-order
321   dilution process demonstrates that the simulation of HOx is rather insensitive to this parameter
322   (Figure S5). In general, the model performance is consistent, or outperforms, results from recent
323   box modeling studies, indicating that it is at least roughly representative of the real-world ozone
324   chemistry and sensitivity regimes.

325   *3.2.   Can HCHO/NO$_2$ ratios fully describe the HOx-ROx cycle?*

326   Kleinman et al. (2001) demonstrated that LROx/LNOx is the most robust ozone regime
327   indicator. Thus, the predictive power of FNR at detecting the underlying chemical conditions can
328   be challenged by comparing FNR to LROx/LNOx. Ideally, if they show a strong degree of
329   correspondence (i.e., R^2=1.0), we can confidently say that FNR can realistically portray the
330   chemical regimes. Any divergence of these two quantities indicates the inadequacy of the FNR
331   indicator. Souri et al. (2020) observed a strong linear relationship between the logarithmic
332   transformed FNR and those of LROx/LNOx. Our analysis in this study will be based on the
333   simulated values to ensure that the relationship is coherent based on a realization from the well-
334   characterized box model. As pointed out by Schroeder et al. (2017) and Souri et al. (2020), a
335   natural logarithm of LROx/LNOx roughly equal to -1.0 (i.e., LROx/LNOx = 0.35-0.37)
336   perceptibly separates VOC-sensitive from NOx-sensitive regimes, which would make this
337   threshold the baseline of our analysis.
338   Figure 3 demonstrates the log-log relationship of LROx/LNOx and FNR, and P(O$_3$), from
339   all four air quality campaigns. The log-log relationships from each individual campaign are shown
340   in Figure S6-S9. We overlay the LROx/LNOx baseline threshold along with two commonly used
341   thresholds for FNR suggested by Duncan et al. (2010); they defined the VOC-sensitive regimes if
342   FNR<1 and the NOx-sensitive ones if FNR>2. Any region undergoing a value between these
343   thresholds is unlabeled and considered to be in a transitional regime. The size of each data point
344   is proportional to the HCHO×NO$_2$ concentration magnitude. One striking finding from this plot is
345   that there is indeed a strong linear relationship between the logarithmic-transformed LROx/LNOx
346   and FNR (R^2=0.91). A strong linear relationship between the two quantities in the log-log scale
347   indicates a power law dependence (i.e., $y=ax^b$). A strong power law dependency means that these
348   two quantities have a poor correlation at their low and high values. This is mainly caused by the
349   fact that HCHO does not fully describe VOC reactivity rates in environments with high and low
350   VOC concentrations (Souri et al., 2020). The question is, what range of FNR will fall in
351   ln(LROx/LNOx) = -1.0±0.2? Following the baseline, the transitioning ratios follow a normal
352   distribution with a mean of 1.8, a standard deviation of 0.4, and a range from 1 to 4 (Figure S10).
353   We define the chemical error in the application of FNR to separate the chemical regimes as the
354   relative error standard deviation (i.e., σ/μ) of the transitioning ratios leading to ~ 20%. These
355   numbers are based on a single model realization and can change if a different mechanism is used;

356 nonetheless, the model has considerable skill at reproducing many different unconstrained
357 compounds, especially OH, suggesting that it is a rather reliable realization. Comparing the
358 transitioning FNRs to the NO_2 concentrations suggests no correlation (r=0.02), whereas there is a
359 linear correlation between the transitioning ratios and the HCHO concentrations (r=0.56). This
360 tendency reinforces the study of Souri et al. (2020), who, primarily due to the HCHO-NO_2
361 feedback, observed a larger FNR threshold in VOC-rich environments to be able to detect the
362 chemical regimes.

3.3.   Large PO_3 rates occur in regions with large HCHO×NO_2 concentrations when moving toward NOx-sensitive regions

365   A striking and perhaps intuitive tendency observed from Figure 3 is that large PO_3 rates
366 are mostly tied to higher HCHO×NO_2. But this relationship gradually weakens as we move
367 towards VOC-sensitive regions (smaller LROx/LNOx ratios). This is a textbook example of non-
368 linear ozone chemistry. In VOC-sensitive areas, PO_3 can be strongly inhibited by NO_2+OH and
369 the formation of organic nitrates despite the abundance of the precursors. In the application of
370 remote-sensing of ozone precursors, the greatest unused metric describing the mass of the ozone
371 precursors is HCHO×NO_2. However, this metric should only be used in conjunction with FNR. To
372 demonstrate this, based on what the baseline (LROx/LNOx) suggests against thresholds on FNRs
373 defined by Duncan et al. (2010), we group the data into four regions: NOx-sensitive – NOx-
374 sensitive, NOx-sensitive–transitional, VOC-sensitive–transitional, and VOC-sensitive–VOC-
375 sensitive. A different perspective on this categorization is that the transitional regimes are a weaker
376 characterization of the main regime; for instance, NOx-sensitive–transitional regions are less NOx-
377 sensitive than NOx-sensitive – NOx-sensitive. Subsequently, the cumulative distribution functions
378 (CDFs) of PO_3 and HCHO×NO_2 with respect to the aforementioned groups are calculated, which
379 is shown in Figure 4. Regarding NOx-sensitive—NOx-sensitive regions, we see the PO_3 CDF very
380 quickly converging to the probability of 100%, indicating that the distribution of PO_3 is skewed
381 towards very low values. The median of PO_3 for this particular regime (where CDF = 50%) is only
382 0.25 ppbv/hr. This agrees with previous studies such as Martin et al. (2002), Choi et al. (2012), Jin
383 et al. (2017), and Souri et al. (2017), reporting that NOx-sensitive regimes dominate in pristine
384 areas. The PO_3 CDFs between NOx-sensitive—transitional and VOC-sensitive—VOC-sensitive
385 are not too distinct, whereas their HCHO×NO_2 CDFs are substantially different. The non-linear
386 ozone chemistry suppresses PO_3 in highly VOC-sensitive areas such that those values are not too
387 different from those in mildly polluted areas (NOx-sensitive—transitional). Perhaps the most
388 interesting conclusion from this figure is that elevated PO_3 values (median = 4.6 ppbv/hr), a factor
389 of two larger than two previous regimes, are mostly found in VOC-sensitive—transitional. This is
390 primarily due to two causes: i) this particular regime is not strongly inhibited by the nonlinear
391 chemistry, particularly NO_2+OH, and ii) it is associated with abundant precursors evident in the
392 median of HCHO×NO_2 being three times as large of those in NOx-sensitive—transitional. This
393 tendency illustrates the notion of non-linear chemistry and how this may affect regulations. Simply
394 knowing where the regimes are might not suffice to pinpoint the peak of PO_3, as this analysis
395 suggests that we need to consider both FNR and HCHO×NO2; both metrics are readily accessible
396 from satellite remote-sensing sensors.

3.4.   *Can we estimate PO_3 using the information from HCHO/NO_2 and HCHO×NO_2?*

398   It may be advantageous to construct an empirical function fitted to these two quantities and
399 elucidate the maximum variance (information) we can potentially gain to recreate PO_3. After
400 several attempts, we found a bilinear function ($z=a_0+a_1x+a_2y+a_3xy$) to be a good fit without

401 overparameterization. Due to presence of extreme values in both FNR and HCHO×NO$_2$, we use a
402 weighted least squares method for the curve fitting based on the distance of the fitted curve to the
403 data points (known as bi-squares weighting). The best fit with R^2 equals to 0.94 and an RMSE of
404 0.60 ppbv/hr is:

$$PO_3 = 0.74 - 0.09\,x - 0.02\,y + 0.25xy \tag{4}$$

405 where x and y are FNR (unitless) and HCHO×NO$_2$ (ppbv^2), respectively. The residual of the fit is
406 shown in Figure S11. The gradients of PO$_3$ with respect to x and y are:

$$\frac{dPO_3}{dx} = 0.25y - 0.09 \tag{5}$$

$$\frac{dPO_3}{dy} = 0.25x - 0.02 \tag{6}$$

407 An apparent observation arises from these equations that is the derivative of PO$_3$ to each
408 metric depends on the other one underscoring their interconnectedness. For instance, Eq. (6)
409 suggests that larger FNRs (x) result in a larger gradient of PO$_3$ to the abundance of HCHO×NO$_2$
410 (y). In very low FNRs, this gradient can become very small, rendering PO$_3$ insensitive (or in
411 extreme cases, negatively correlated) to HCHO×NO$_2$. This analysis provides encouraging results
412 about the future application of the satellite-derived HCHO×NO$_2$; however, the wide class of
413 problems relating to the application of satellite-derived FNR columns, such as satellite errors in
414 columns or the translation between columns to PBL is also present in Eq. (4), even in a more
415 pronounced way due to HCHO×NO$_2$ and HCHO^2 (= xy). This new perspective on PO$_3$ estimation
416 deserves a separate study.

3.5. Altitude dependency and its parametrization

418 A lingering concern over the application of satellite-based FNR tropospheric columns is
419 that the vertical distribution of HCHO and NO$_2$ are integrated into columns; thus, this vertical
420 information is permanently lost. Here, we provide insights into the vertical distribution of FNR
421 within the tropospheric column. This task requires information about the differences between i)
422 the vertical shape of HCHO and that of NO$_2$ and ii) the vertical shape in the sensitivity of the
423 retrievals to the different altitude layers (described as scattering weights). Ideally, if both
424 compounds show an identically relative shape, the FNR columns will be valid for every air parcel
425 along the vertical path (i.e., a straight line). Previous studies such as Jin et al. (2017) and Schroeder
426 et al. (2017) observed a large degree of vertical inhomogeneity in both HCHO and NO$_2$
427 concentrations suggesting that this ideal condition cannot be met. We do not always have precise
428 observations of HCHO and NO$_2$ vertical distributions, but we can constitute some degree of
429 generalization by leveraging the measurements made during the aircraft campaigns. As for the
430 differences in the vertical shapes (i.e., the curvature) of the sensitivity of the retrievals between
431 HCHO and NO$_2$ channels (i.e., ~ 340 nm and ~440 nm), under normal atmospheric and viewing
432 geometry conditions, several studies such as Nowlan et al. 2018 and Lorente et al. 2017 showed
433 small differences in the vertical shapes of the scattering weights in the first few kilometers altitude
434 above the surface where the significant fluctuations in FNRs usually take place. Therefore, our
435 analysis does not consider the varying vertical shapes in the scattering weights. However, this
436 assumption might not hold for excessive aerosol loading with variable extinction efficiency
437 between ~340 nm and ~440 nm wavelengths or extreme solar zenith angles.
438 Figure 5 demonstrates the violin plot of the afternoon (> 12:00 LT) vertical distribution of
439 HCHO, NO$_2$, and FNR observed by NASA's aircraft during the four field campaigns analyzed in
440 this study superimposed by the simulated PO$_3$ rates. The vertical layers are grouped into sixteen

441   altitudes ranging from 0.25 km to 7.75 km. Each vertical layer incorporates measurements ±0.25
442   km of the mid-layer height. The observations do not follow a normal distribution, particularly in
443   the lower parts of the atmosphere; thus, medians are preferred to represent the central tendency.
444   While the largest PO_3 rates tend to occur in areas close to the surface (< 2 km agl), a nonnegligible
445   fraction of the elevated PO_3 rates are also observed in other parts of the atmosphere, such as in the
446   free troposphere.
447   Several intriguing features are observed in Figure 5: First, up to the 5.75 km range, which
448   encompasses the PBL area and a large portion of the free troposphere, NO_2 concentrations tend to
449   decrease quicker than those of HCHO in line with previous studies such as Schroeder et al. (2017),
450   Jin et al. (2017), Chan et al. (2019), and Ren et al. (2022). Second, above 5.75 km, HCHO levels
451   off, whereas NO_2 shows an increasing trend. Finally, due to their different vertical shapes, we
452   observe nonuniformities in the vertical distribution of FNR: they become more NOx-sensitive with
453   altitude up to a turning point at 5.75 km and then shift back to the VOC-sensitive direction.
454   It is attractive to model these shapes and apply parameterizations to understand how their
455   shapes will complicate the use of tropospheric column retrieval from satellites. First order rational
456   functions are a good candidate to use. Concerning the vertical dependency of HCHO and NO_2, we
457   find reasonable fit (R^2=0.73) as:

$$HCHO, NO_2 = \frac{a_0 z + a_1}{z + a_2} \qquad (7)$$

458   where z is altitude in km. a_i (i=0,1,2) are fitting parameters. From this equation it is determined
459   that FNRs follow a second order rational function:

$$f(z) = \frac{HCHO}{NO_2} = \frac{b_0 z^2 + b_1 z + b_2}{b_3 z^2 + b_4 z + b_5} \qquad (8)$$

460   where b_i (i=0, … , 5) are fitting parameters. One can effortlessly fit this function to different bounds
461   of the vertical distribution of FNR such as the 25th and 75th percentiles, and subsequently estimate
462   the first moment of the resultant polygon along z divided by the total area bounded to the polygon
463   (the centroid, G) via:

$$G(z_1, z_2) = \frac{1}{2A} \int_{z1}^{z2} f^2(z)_{75th} - f^2(z)_{25th} \, dz \qquad (9)$$

464   where A is the area of the polygon bounded by the 75th percentiles, $f(z)_{75th}$, and the 25th
465   percentiles ($f(z)_{25th}$) of FNR (shown in Figure 5 as solid black lines). We define an altitude
466   adjustment factor (f_{adj}) such that one can translate an observed FNR tropospheric column ratios,
467   such as those retrieved from satellites, to a defined altitude and below that point (zt) through:

$$f_{adj} = \frac{G(0, z_t)}{G(0, 8 \, km)} \qquad (10)$$

468   where zt can be interchanged to match the PBLH. This definition is more beneficial than using the
469   entire tropospheric column to the surface conversion (e.g., Jin et al., 2017) because ozone can form
470   in various vertical layers. Using the observations collected during the campaign, we estimate Eq.
471   (10) along with ±1σ boundaries shown in Figure 6. To determine the adjustment factor error, we
472   reestimate Eq.9 with ±1σ level in the coefficients obtained from Eq.8. The resultant error is shown
473   in the dashed red line in Figure 6. This error results from uncertainties associated with assuming
474   that the second-order rational function can explain the vertical distribution of FNRs. The shape of
475   the resulting adjustment factor is in line with the vertical distribution of FNR (see Figure 5): the
476   adjustment factor curve closer to the surface has values smaller than one, increases to values larger
477   than one in the mid-troposphere, and finally, converges to one near the top of measured
478   concentrations. If one picks out an altitude pertaining to a PBLH, one can easily apply f_{adj} to the

479 observed FNR columns to estimate the corresponding ratio for that specific PBLH. A more evolved
480 PBLH (i.e., a large zt) results in stronger vertical mixing, rendering f_{adj} closer to one. The standard
481 error deviation of this conversion is around 19%. The relatively low fluctuations in the adjustment
482 factor around one suggest that under the observed atmospheric conditions (clear-sky afternoon
483 summers), the columnar tropospheric ratios do not poorly represent the chemical conditions in the
484 PBL region.
485   It is beneficial to model this curve to make this data-driven conversion easier for future
486 applications. A second-order polynomial can well describe (R^2=0.97) this curve:

$$f_{adj} = az_t^2 + bz_t + c \qquad\qquad a = -0.01, b = 0.15, c = 0.78 \qquad\qquad (11)$$

487 Although Eq. (11) does not include observations above 8 km, the area bounded between $f(z)_{75th}$
488 and $f(z)_{25th}$ in higher altitudes is too small to make a noticeable impact on this adjustment factor.
489   One may object that since we estimated the adjustment factor based on two boundaries
490 (25th and 75th percentiles) of the data, we are no longer really dealing with 50% of features
491 observed in the vertical shapes of FNR. This valid critique can be overcome by gradually relaxing
492 the lower and upper limits and examining the resulting change in f_{adj}. When we reduce the lower
493 limit in Eq. (9) from the 25th to 1st percentiles, the optimal curve is similar to the one shown in
494 Figure 6 (Figure S12). However, when we extend the upper limit from the 75th percentile to greater
495 values, we see the fit becoming less robust above the 80th percentile, indicating that the formulation
496 applies to ~80% of the data. The reason behind the poor representation of the adjustment factor
497 for the upper tail of the population is the extremely steep turning point between 5.5 and 6.0 km,
498 necessitating a higher-order rational function to be used for Eq. (7) and Eq. (8). We prefer to limit
499 this analysis to both boundaries and the order defined in Eq. (8) and Eq. (9) because extreme value
500 predictions usually lack robustness.
501   A caveat with these results is that our analysis is limited to afternoon observations because
502 we focus on afternoon low-orbiting sensors such as OMI and TROPOMI. Nonetheless, Schroeder
503 et al. (2017) and Crawford et al. (2021) observed large diurnal variability in these profiles due to
504 diurnal variability in sinks and sources of NO_2 and HCHO and atmospheric dynamics. The diurnal
505 cycle has an important implication for geostationary satellites such as Tropospheric Emissions
506 indeed: Monitoring of Pollution (TEMPO) (Chance et al., 2019). Limiting the observations to
507 morning time results in a smaller adjustment factor for altitudes close to the surface resulting from
508 steeper vertical gradients of HCHO/NO_2 (Figures S13 and S14). This tendency agrees with Jin et
509 al. (2017), who observed a larger deviation from one in an adjustment factor used for the column-
510 surface conversion in winter.
511   Another important caveat with our analysis is that it is based upon four air quality
512 campaigns in warm seasons that avoid times/areas with convective transport; as such, our analysis
513 needs to be made aware of the vertical shapes of FNR during convective activities and cold
514 seasons. However, a few compelling assumptions can minimize these oversights: first, it is very
515 atypical to encounter elevated ozone production rates during cold seasons with few exceptions
516 (Ahmadov et al., 2015; Rappenglück et al., 2014); second, the notion of ozone regimes is only
517 appropriate in photochemically active environments where the ROx-HOx cycle is active; an
518 example of this can be found in Souri et al. (2021) who observed an enhancement of surface ozone
519 in central Europe during a lockdown in April 2020 (up to 5 ppbv) compared to a baseline which
520 was explainable by the reduced O_3 titration through NO in place of the photochemically induced
521 production. An exaggerated extension to this example is the nighttime chemistry where NO-O_3-
522 NO_2 partitioning is the primary driver of negative ozone production rates; at night, the definition
523 of NOx-sensitive or VOC-sensitive is meaningless, so it is in photochemically less active

524 environments; third, it is rarely advisable to use cloudy scenes in satellite UV-Vis gas retrievals
525 due to the arguable assumption on Lambertian clouds and highly uncertain cloud optical centroid
526 and albedo; accordingly, atmospheric convection occurring during storms or fires is commonly
527 masked in satellite-based studies. Therefore, the limitations associated with the adjustment factor
528 are mild compared to the advantages.

3.6.   Spatial Heterogeneity

530   The spatial representation error resulting from unresolved processes and scales (Janić et
531 al., 2016; Valin et al., 2011; Souri et al., 2022) refers to the amount of information lost due to
532 satellite footprint or unresolved inputs used in satellite retrieval algorithms. Unfortunately, this
533 source of error cannot be determined when we do not know the true state of the spatial variability.
534 There is, however, a practical way to resolve this by conducting multi-scale intercomparisons of a
535 coarse spatial resolution output against a finer one. Yet, despite the absence of the truth in this
536 approach, we tend to find their comparisons useful in giving us an appreciation of the error.
537   We build the reference data on qualified pixels (qa_value> 0.75) of offline TROPOMI
538 tropospheric NO_2 version 2.2.0 (van Geffen et al., 2021; Boersma et al., 2018) and total HCHO
539 columns version 2.02.01 (De Smedt et al., 2018) oversampled at 3×3 km^2 in summer 2021 over
540 the US. Figure 7 shows the map of those tropospheric columns as well as FNR. Encouragingly,
541 the small footprint and relatively low detection limit of TROPOMI compared to its predecessor
542 satellite sensors (e.g., OMI) enable us to have possibly one of the finest maps of HCHO over the
543 US to date. Large values of HCHO columns are found in the southeast due to strong isoprene
544 emissions (e.g., Zhu et al., 2016; Wells et al., 2020). Cities like Houston (Boeke et al., 2011; Zhu
545 et al., 2014; Pan et al., 2015; Diao et al., 2016), Kansas City, Phoenix (Nunnermacker et al., 2004),
546 and Los Angeles (de Gouw et al., 2018) also show pronounced enhancements of HCHO possibly
547 due to anthropogenic sources. Expectedly, large tropospheric NO_2 columns are often confined to
548 cities and some coal-fired power plants along the Ohio River basin. Concerning FNR, low values
549 dominate cities, whereas high values are found in remote regions. An immediate tendency
550 observed from these maps is that the length scale of HCHO columns is longer than that of NO_2.
551 This indicates that NO_2 columns are more heterogeneous. Because of this, we observe a large
552 degree of spatial heterogeneity with respect to FNRs.
553   Here we limit our analysis to Los Angeles due to computational costs imposed by the
554 subsequent experiment. To quantify the spatial representation errors caused by satellite footprint
555 size, we upscale the FNRs by convolving the values with four low pass box filters with the size of
556 13×24, 36×36, 108×108, and 216×216 km^2, shown in the first column of Figure 8. Subsequently,
557 to extract the spatial variance (information), we follow the definition of the experimental
558 semivariogram (Matheron, 1963):

$$\gamma(\boldsymbol{h}) = \frac{1}{2N(\boldsymbol{h})} \sum_{|x_i - x_j| - |\boldsymbol{h}| \leq \varepsilon} [Z(x_i) - Z(x_j)]^2 \tag{12}$$

559 where $Z(x_i)$ (and $Z(x_j)$) is discrete pixels of FNRs, $N(\boldsymbol{h})$ is the number of paired pixels separated
560 by the vector of $\boldsymbol{h}$. The |.| operator indicates the length of a vector. The condition of $|x_i - x_j| -$
561 $|\boldsymbol{h}| \leq \varepsilon$ is to permit certain tolerance for differences in the length of the vector. Here, we ignore
562 the directional dependence in $\gamma(\boldsymbol{h})$ which makes the vector of $\boldsymbol{h}$ scalar ($h = |\boldsymbol{h}|$). Moreover, we bin
563 γ values in 100 evenly-spaced intervals ranging from 0 to 5 degrees. To remove potential outliers
564 (such as noise), it is wise to model the semivariogram using an empirical regression model. To
565 model the semivariogram, we follow the stable Gaussian function used by Souri et al. (2022):

$$\gamma(h) = s(1 - e^{-(\frac{h}{r})^{c_0}}): c_0 = 1.5 \tag{13}$$

566 where r and s are fitting parameters. For the most part, geophysical quantities become spatially
567 uncorrelated at a certain distance called the range, and the variance associated with that distance
568 is called the sill. The fitting parameters, r, and s, describe these two quantities as long as the stable
569 Gaussian function can well fit to the shape of semivariogram. The semivariograms, and the fits,
570 associated with each map are depicted in the second column of Figure 8.

571   The modeled semivariograms suggest that a coarser field comes with a smaller sill,
572 implying a loss in the spatial information (variance). The length scale (i.e., the range) only sharply
573 increases at coarser footprints ($>36\times36$ km^2). This indicates that several coarse-resolution satellite
574 sensors, such as OMI (13×24 km^2), are rather able to determine the length scales of FNR over a
575 major city such as Los Angeles. By leveraging the modeled semivariograms, we can effortlessly
576 determine the spatial representation error for specific scale (e.g., h=10 km) through

$$e^2(h) = 1 - \frac{\gamma(h)}{\gamma_{ref}(h)} \tag{14}$$

577 where $\gamma(h)$ and $\gamma_{ref}(h)$ are the modeled semivariogram of the target and the reference fields (3×3
578 km^2). This equation articulates the amount of information lost in the target field compared to the
579 reference. Accordingly, the proposed formulation of the spatial representation error is relative.
580 Figure 9 depicts the representation errors for various footprints. For the most part, the OMI nadir
581 pixel (13×24 km^2) only has a ~12% loss of the spatial variance. On the contrary, a grid box with a
582 size of 216×216 km^2 fails at capturing ~65% of the spatial information in FNR with a 50 km length
583 scale comparable to the extent of Los Angeles. The advantage of our method is that we can
584 mathematically describe the spatial representation error as a function of the length of our target.
585 The present method can be easily applied to other atmospheric compounds and locations. We have
586 named this method SpaTial Representation Error EstimaTor (STREET) which is publicly available
587 as an open-source package (Souri, 2022).

588   An oversight in the above experiment lies in its lack of appreciation of unresolved physical
589 processes in the satellite measurements: a weak sensitivity of some retrievals to the near-surface
590 pollution due to the choice of spectral windows used for fitting (Yang et al., 2014), using 1-D air
591 mass factor calculation instead of 3-D (Schwaerzel et al., 2020), and neglecting aerosol effect on
592 the light path are just a few examples to point out. To account for the unresolved processes, one
593 can recalculate Eqs. (12)-(14) using outputs from different retrieval frameworks, which is beyond
594 the scope of this study.

3.7. Satellite errors

3.7.1. Concept

597   Two types of retrieval errors can affect our analysis: systematic errors (bias) and
598 unsystematic ones (random errors). In theory, it is very compelling to understand their differences.
599 In reality, the distinction between random and systematic errors is not as clear-cut as it seems. For
600 example, one may wish to establish the credibility of a satellite retrieval by comparing it to a sky-
601 radiance measurement over time. Because each measurement is made at a different time, their
602 comparison is not a repetition of the same experiment; each time, the atmosphere differs in some
603 aspects, so each comparison is unique. Adding more sky-radiance measurements will add new
604 experiments. For each paired data point, many unique issues contribute differently to errors; as
605 such, our problem is grossly under-determined (i.e., more unknowns for a given observation).

606 Here, we do not attempt to separate random from systematic errors in the subsequent analysis,
607 thereby limiting this study to the total uncertainty.

608 We focus on analyzing the statistical errors drawn from the differences between the
609 benchmark and the retrievals on daily basis. Two sensors are used for this analysis: TROPOMI
610 and OMI. To propagate individual uncertainties in HCHO and NO_2 to FNRs, we follow an
611 analytical approach involving Jacobians of the ratio to HCHO and NO_2. Assuming that errors in
612 HCHO and NO_2 are uncorrelated, the relative error of the ratio can be estimated by:

$$\frac{\sigma}{ratio} = \sqrt{\left(\frac{\sigma_{HCHO}}{HCHO}\right)^2 + \left(\frac{\sigma_{NO_2}}{NO_2}\right)^2} \qquad (15)$$

613 where σ_{HCHO} and σ_{NO_2} are total uncertainties of HCHO and NO_2 observations. It is important to
614 recognize that the errors in HCHO and NO_2 are not strictly uncorrelated due to assumptions made
615 in their air mass factor calculations.

3.7.2. Error Distributions in TROPOMI and OMI

617 We begin our analysis with the error distribution of daily TROPOMI tropospheric NO_2
618 columns (v1.02.02) against 22 MAX-DOAS instruments from May to September in 2018-2021.
619 The data are paired based on the criteria defined in Verhoelst et al. (2021). The spatial locations
620 of the stations are mapped in Figure S15. Figure 10a shows the histogram of the TROPOMI minus
621 the MAX-DOAS instruments. The first observation from this distribution is that it is skewed
622 towards lower differences, evident in the skewness parameter around -4.6. As a result of the
623 skewness, the median should better represent the central tendency which is around -1×10^{15}
624 molec./cm^2. In general, TROPOMI tropospheric NO_2 columns show a low bias. We fit a normal
625 distribution to the data using the non-linear Levenberg-Marquardt method. This fitted normal
626 distribution (R^2=0.94) is used to approximate σ_{NO_2} for different confidence intervals, and to
627 minimize blunders. To understand how much of these disagreements are caused by systematic
628 errors as opposed to random errors, we redo the histogram using monthly-based observations
629 (Figure S16). A slight change in the dispersions between the daily and the monthly-basis analysis
630 indicates the significance of unresolved systematic (or relative) biases. This tendency suggests that
631 when conducting the analysis on a monthly basis, the relative bias cannot be mitigated by
632 averaging. Verhoelst et al. (2021) rigorously studied the potential root cause of some discrepancies
633 between MAX-DOAS and TROPOMI. An important source of error stems from the fundamental
634 differences in the vertical sensitivities of MAX-DOAS (more sensitive to the lower tropospheric
635 region) and TROPOMI (more sensitive to the upper tropospheric area). This systematic error can
636 only be mitigated using reliably high-resolution vertical shape factors instead of spatiotemporal
637 averaging of the satellite data.

638 The error analysis for OMI follows the same methods applied for TROPOMI; however,
639 with different benchmarks. We follow the comparisons made between the operational product
640 version 3.1 and measured columns derived from NCAR's NO_2 measurements integrated along
641 aircraft spirals during four NASA's air quality campaigns. More information regarding this data
642 comparison can be found in Choi et al. (2020). Figure 10b shows the histogram of OMI minus the
643 integrated spirals. Compared to TROPOMI, the OMI bias is worse by a factor of two. The standard
644 deviation calculated from a Gaussian fit (2.31×10^{15} molec./cm^2) is not substantially different from
645 that of TROPOMI (2.11×10^{15} molec./cm^2).

646 As for the error distribution of TROPOMI HCHO columns (version 1.1.(5-7)), we use 24
647 FTIR measurements during the same time period based on the criteria specified in Vigouroux et

al. (2020). The stations are mapped in Figure S15. The frequency of the paired data is daily. Figure 11a depicts the error distribution. The distribution is slightly broader compared to that of NO$_2$, manifested in a larger standard deviation 4.32×10^{15} molec./cm^2. This is primarily due to two facts: i) HCHO optical depths generally peak in the UV range (<380 nm), where the large optical depths of ozone and Rayleigh scattering result in weaker and noisier signals (Gonzalez Abad et al., 2019), and ii) the broader and stronger NO$_2$ optical depths in the ViS range (400-500 nm), where the signal-to-noise ratio is typically more outstanding, permit better quality retrievals. Similar to the NO$_2$, we fit a normal distribution (R^2=0.90) to specify σ_{HCHO} for different confidence intervals.

Concerning OMI HCHO columns from SAO version 3 (Gonzalez Abad et al., 2015), we follow the intercomparison approach proposed in Zhu et al. (2020). Based on this approach, the benchmarks come from GEOS-Chem simulated HCHO columns corrected by in-situ aircraft measurements. The measurements were made during ozone seasons from KORUS-AQ, DISCOVERs, FRAPPE, NOMADSS, and SENEX campaigns (see Table 1 in Zhu et al. 2020). OMI values ranging from -0.5×10^{15} molec./cm^2 and 1.0×10^{17} molec./cm^2 with effective cloud fraction between 0.0 and 0.3, and SZA between 0 and 60 degrees are only considered in the comparison. Any pixels from OMI and grid boxes from the corrected GEOS-Chem simulation that fall into a polygon enclosing the campaign domain are used to create the error distribution shown in Figure 11b. The distribution has much denser data because the model output covers a large portion of the satellite swath. The error distribution suggests that OMI HCHO is inferior to TROPOMI evident in larger bias and standard deviation. The OMI bias is twice as large as that of TROPOMI. De Smedt et al. (2021) observed the same level of bias from their comparisons of OMI/TROPOMI with MAX-DOAS instruments (see Table 3 in their paper). Moreover, their OMI vs MAX-DOAS comparisons were severely scattered. Likewise, we observe the standard deviation of OMI from the fitted Gaussian function to be roughly five times as large of that TROPOMI. This can be primarily due to a weaker signal-to-noise (and sensor degradation) in OMI. It is because of this reason that OMI HCHO should be averaged over several months. Another possible reason for the large standard deviation is the fact that the benchmark arises from a modeling experiment whose ability at resolving spatiotemporal variations in HCHO may be uncertain. This partly leads to the performance of OMI to look poor.

3.7.3.   The impact of retrieval error on the ratio

Following Eq. (15), we calculate the standard error for a wide range of NO$_2$ and HCHO columns at a 68% confidence interval (1 sigma) for both TROPOMI and OMI derived from the fitted Gaussian function to the histograms; the standard errors are shown in Figure 12. We observe smaller errors to be associated with larger tropospheric column concentrations. As for TROPOMI, either daily HCHO or tropospheric NO$_2$ columns should be above 1.2-1.5×10^{16} molec./cm^2 to achieve 20-30% standard error. The TROPOMI errors start diminishing the application of FNR when both measurements are below this threshold. Regarding OMI, it is nearly impossible to get the standard error below of 20-30% given its problematically large HCHO standard deviation. For 50% error, the daily HCHO columns should be above 3.2×10^{16} molec./cm^2. This range of error can also be achieved if OMI tropospheric NO$_2$ columns are above 8×10^{15} molec./cm^2.

3.8.   The fractional errors to the combined error

The ultimate task is to compile the aforementioned errors to gauge how each individual source of error contributes to the overall error. Although each error is different in nature, combined they explain the uncertainties of one quantity (FNR) and can be roughly considered independent; therefore, the combined error is given by:

16

$$\sigma_{total} = \sqrt{\sigma_{Col2PBL}^2 + \sigma_{SpatialRep}^2 + \sigma_{Retreival}^2} \tag{16}$$

$\sigma_{Col2PBL}$ is the error in the adjustment-factor defined in this study. We calculated a 26% standard error for a wide range of PBLHs. Therefore, $\sigma_{Col2PBL}$ equals to 26% of the observed ratio (i.e., magnitude dependent). $\sigma_{SpatialRep}$ is more complex. It is a function of the footprint of the satellite (or a model), the spatial variability of the reference field, which varies from environment to environment, and the length scale of our target (e.g., a district, a city, or a state). Eq. (14) explicitly quantifies this error. The product of the square root of that value and the observed ratio defines $\sigma_{SpatialRep}$. The last error depends on the magnitude of HCHO and NO_2 tropospheric columns. It can be estimated from Eq. (15) times the observed ratio. We did not include the chemistry error in Eq. (16) because it was suited only for segregating the chemical conditions; it does not describe the level of uncertainties that comes with the observed columnar ratio. Figure 13 shows the total relative error given the observed TROPOMI ratio seen in Figure 7. We consider the OMI spatial representation error (13% variance loss) for this case that was computed in a city environment. The retrieval errors are based on TROPOMI sigma values. Areas associated with relatively small errors (<50%) are mostly seen in cities due to a stronger signal (smaller $\sigma_{Retreival}$). Places with low vegetation and anthropogenic sources (i.e., Rocky Mountains) possess the largest errors (>100%).

To produce some examples of the fractional errors to the combined error, we focus on two different environments with two different sets of HCHO and NO_2 columns. One represents a heavily polluted area, and the other one is a moderately polluted region. We also include two footprints: OMI (13×24 km^2) and a 108×108 km^2 pixel. Finally, we calculate the percentage of each error component for both OMI and TROPOMI sensors. Figure 14 shows the pie charts describing the percentage of each individual error to the total error for TROPOMI. Unless the footprint of the sensor is coarse enough (e.g., 108 km^2) to give rise to the spatial representation error dominance, the retrieval error stands out. New satellites are not expected to have very large footprints; as such, retrieval errors appear to be the major obstacle to using FNR in a robust manner. Figure 15 shows the same calculation but using OMI errors; the retrieval errors massively surpass other errors. This motivates us to do one more experiment; we recalculate the HCHO error distribution in OMI using monthly-averaged data instead of daily (Figure S17). This experiment suggests a standard deviation of 9.4×10^{15} molec./cm^2, with which we again observe the retrieval error to be the largest contributor (>80%) of the combined error (Figure S18). A recent study (Johnson et al., 2022) also suggests that retrieval errors can result in considerable disagreement between FNRs from various sensors and retrieval frameworks.

4. Summary

The main goal of this study was to characterize the errors associated with the ratio of satellite-based HCHO to NO_2 columns, which has been widely used for ozone sensitivity studies. From the realization of the complexity of the problem, we now know that four major errors should be carefully quantified so that we can reliably represent the underlying ozone regimes. The errors are broken down into i) the chemistry error, ii) the column to the PBL translation, iii) the spatial representation error, and iv) the retrieval error. Each error has its own dynamics and has been tackled differently by leveraging a broad spectrum of tools and data.

The chemistry error refers to the predictive power of the HCHO/NO_2 ratio (hereafter FNR) in describing the HOx-ROx cycle, which can be well explained by the ratio of the chemical loss

735   of HO_2+RO_2 (LROx) to the chemical loss of NOx (LNOx). Because those chemical reactions are
736   not directly observable, we set up a chemical box model constrained with a large suite of in-situ
737   aircraft measurements collected during DISCOVER-AQs and KORUS-AQ campaigns (~ 500 hr
738   of flight). Our box model showed a reasonable performance at recreating some unconstrained key
739   compounds such as OH (R^2=0.64, bias=17%), HO_2 (R^2=0.66, bias<1%), and HCHO (R^2=0.73).
740   Subsequently, we compared the simulated FNRs to LROx/LNOx. They showed a high degree of
741   correspondence (R^2=0.93) but only in the logarithmic scale; this indicated that FNRs do not fully
742   describe the HOx-ROx cycle (i.e., the sensitivity of ozone production rates to NOx and VOC) for
743   heavily polluted environments and pristine ones. Following a robust baseline indicator
744   (ln(LROx/LNOx) = -1.0 ± 0.2) segregating NOx-sensitive from VOC-sensitive regimes, we
745   observed a diverse range of FNR ranging from 1 to 4. These transitioning ratios had a Gaussian
746   distribution with a mean of 1.8 and a standard deviation of 0.4. This implied that the relative
747   standard error associated with the ratio from the chemistry perspective at a 68% confidence interval
748   was 20%. Although this threshold with its error was based on a single model realization and can
749   be different for a different chemical mechanism, it provided a useful universal baseline derived
750   from various chemical and meteorological conditions. At a 68% confidence level, any uncertainty
751   beyond 20% in the ozone regime identification from FNRs likely originates from other sources of
752   error, such as the retrieval error.
753   Results from the box model showed that ozone production rates in extremely polluted
754   regions (VOC-sensitive) were not significantly different from those in pristine ones (NOx-
755   sensitive) due to non-linear chemical feedback mostly imposed by NO_2+OH. Indeed, the largest
756   PO_3 rates (median = 4.6 ppbv/hr) were predominantly seen in VOC-sensitive regimes tending
757   towards the transitional regime. This was primarily caused by the abundance of ozone precursors
758   (i.e., HCHO×NO_2) and the diminished negative chemical feedback. We also revealed that
759   HCHO×NO_2 could be used as a sensible proxy for the ozone precursors' abundance. In theory,
760   this metric, in conjunction with the ratio, provided reasonable estimates of PO_3 rates (RMSE =
761   ±0.60 ppbv/hr).
762   We then analyzed the afternoon vertical distribution of HCHO, NO_2, and their ratio
763   observed from aircraft during the air quality campaigns binned to the near-surface to 8 km. For
764   altitudes below 5.75 km, HCHO concentration steadily decreased with altitude but at a lower rate
765   than NO_2. Above that altitude, NO_2 concentrations stabilized and slightly increased due to
766   lightning and stratospheric sources. The dissimilarity between the vertical shape of NO_2 versus
767   HCHO resulted in a rather non-linear shape of FNR. This non-linear shape necessitated a
768   mathematical formulation to transform an observed columnar ratio to a ratio at a desired vertical
769   height expanding from the surface. We fit a second-order rational function to the profile and
770   formulated the altitude adjustment factor, which followed a second-order polynomial function
771   starting from values below 1 for lower altitudes, following values above 1 for some high altitudes,
772   and finally converging to 1 at 8 km. This behavior means that the ozone regime tends to get pushed
773   slightly towards the VOC-sensitive regime near the surface for a given tropospheric columnar
774   ratio. This tendency was more pronounced in morning times when the non-linear shape of FNRs
775   was stronger. This data-driven adjustment factor exclusively derived from afternoon aircraft
776   profiles during warm seasons in non-convective conditions had a standard error of 19%.
777   An important error in the satellite-based observations stemmed from unresolved spatial
778   variability in trace gas concentrations within a satellite pixel (Souri et al., 2022; Tang et al., 2021).
779   The amount of unresolved spatial variability (the spatial representation error) can in principle be
780   modeled if we base our reference on a distribution map made from a high spatial resolution dataset.

781   We modeled semivariograms (or spatial auto-correlation) computed for a reference map of FNR
782   observed by TROPOMI at 3×3 km^2 over Los Angeles. Subsequently, we coarsened the map to
783   13×24, 36×36, 108×108, and 216×216 km^2 and modeled their semivariograms. As for 13×24 km^2,
784   which is equivalent to the OMI nadir spatial resolution, around 12% of spatial information
785   (variance) was lost due to its footprint. The larger the footprint, the bigger the spatial representation
786   error. For instance, a grid box with a size of 216×216 km^2 lost 65% of the spatial information in
787   the ratio at a 50 km length scale. Our method is compelling to understand and easy to apply for
788   other products and different atmospheric environments. Based on this approach, we developed an
789   open-source package called SpaTial Representation Error EstimaTor (STREET) (Souri, 2022).
790   We presented estimates of retrieval errors associated with daily TROPOMI and OMI
791   tropospheric NO_2 columns by comparing them against a large suite of MAX-DOAS (Verhoelst et
792   al. 2021) and vertically-integrated measurements from aircraft spirals (Choi et al., 2020). Both
793   products were smaller than the benchmark. Furthermore, they show a relatively consistent
794   dispersion at a 68% confidence level (~2×10^{15} molec./cm^2) suggested by fitting a normal function
795   (R^2>0.9) to their error distributions. As for daily TROPOMI and OMI HCHO products, we used
796   global FTIR observations (Vigouroux et al., 2020) and data-constrained GEOS-Chem outputs from
797   multiple campaigns (Zhu et al., 2020), respectively. TROPOMI HCHO indeed outperforms OMI
798   HCHO with respect to bias and dispersion on a daily basis. The standard deviation of OMI HCHO
799   was found to be roughly five times as large compared to TROPOMI. While this error can be partly
800   reduced by oversampling over a span of a month or a season, it is critical to recognize that ozone
801   events are episodic; thus, daily observations should be the standard mean for understanding the
802   chemical pathways for the formation of tropospheric ozone. After combining the daily biases from
803   both HCHO and NO_2 TROPOMI comparisons, we concluded that either daily HCHO or
804   tropospheric NO_2 columns should be above 1.2-1.5×10^{16} molec./cm^2 to achieve 20-30% standard
805   error in the ratio. Due to the large error in daily OMI HCHO, it was nearly impossible to achieve
806   20-30% standard error given the observable range of HCHO and NO_2 columns over our planet. To
807   reach 50% error using daily OMI data, HCHO columns should be above 3.2×10^{16} molec./cm^2 or
808   tropospheric NO_2 columns should be above 8×10^{15} molec./cm^2.
809   To build intuition in the significance of the errors above, we finally calculated the
810   combined error in the ratio by linearly combining the root sum of the squares of the TROPOMI
811   retrieval errors, the spatial representation error pertaining to OMI nadir footprint over a city-like
812   environment, and the altitude adjustment error for a wide range of observed HCHO and NO_2
813   columns over the US. These observations were based on the TROPOMI in the summertime of
814   2021. The total errors were relatively mild (<50%) in cities due to a stronger signal, whereas they
815   easily exceeded 100% in regions with low vegetation and anthropogenic sources (i.e., Rocky
816   Mountains). The retrieval error was the dominant source of the combined error (40-90%).
817   All of these aspects highlight the necessity of improving the trace gas satellite retrieval
818   algorithms in conjunction with sensor calibration, although with the realization that a better
819   retrieval is somewhat limited by the advancements made in other disciplines, such as atmospheric
820   modeling and molecular spectroscopy.

Data Access
The FTIR and MAXDOAS data used in this publication were partly obtained from the Network for the Detection of Atmospheric Composition Change (NDACC) and are available through the NDACC website www.ndacc.org. The spatial representation error is estimated based on publicly available package, SpaTial Representation Error EstimaTor (STREET) (https://github.com/ahsouri/STREET). DISCOVER-AQ and KORUS-AQ aircraft data can be downloaded from https://www-air.larc.nasa.gov/missions/discover-aq/discover-aq.html and https://www-air.larc.nasa.gov/missions/korus-aq/. TROPOMI NO_2 and HCHO data can be downloaded from https://disc.gsfc.nasa.gov/datasets/S5P_L2__NO2____1/summary and https://disc.gsfc.nasa.gov/datasets/S5P_L2__HCHO___1/summary. The box model results can be obtained by contacting the corresponding author through ahsouri@cfa.harvard.edu.

Author contributions

AHS designed the research, analyzed the data, conducted the simulations, made all figures, and wrote the paper. MSJ, SP, XL, and KC helped with conceptualization, fundraising, and analysis. GMW helped with configuring the box model. AF, AW, WB, DRB, AJW, RCC, KM, and CC measured various compounds during the air quality campaigns. JHC orchestrated all these campaigns and contributed to the model interpretation. TV, SC, and GP provided paired MAX-DOAS and TROPOMI tropospheric NO_2 observations. CV and BL provided paired FTIR and TROPOMI HCHO observations. SC and LL provided paired integrated aircraft spirals and OMI tropospheric NO_2 observations. LZ and SS provided the paired observations between the corrected GEOS-Chem HCHO and OMI HCHO columns. All authors contributed to the discussion and edited the paper.

References

Ahmadov, R., McKeen, S., Trainer, M., Banta, R., Brewer, A., Brown, S., Edwards, P.M., de Gouw, J.A., Frost, G.J., Gilman, J., Helmig, D., Johnson, B., Karion, A., Koss, A., Langford, A., Lerner, B., Olson, J., Oltmans, S., Peischl, J., Pétron, G., Pichugina, Y., Roberts, J.M., Ryerson, T., Schnell, R., Senff, C., Sweeney, C., Thompson, C., Veres, P.R., Warneke, C., Wild, R., Williams, E.J., Yuan, B., Zamora, R., 2015. Understanding high wintertime ozone pollution events in an oil- and natural gas-producing region of the western US. Atmospheric Chemistry and Physics 15, 411–429. https://doi.org/10.5194/acp-15-411-2015

Bela, M.M., Barth, M.C., Toon, O.B., Fried, A., Ziegler, C., Cummings, K.A., Li, Y., Pickering, K.E., Homeyer, C.R., Morrison, H., Yang, Q., Mecikalski, R.M., Carey, L., Biggerstaff, M.I., Betten, D.P., Alford, A.A., 2018. Effects of Scavenging, Entrainment, and Aqueous Chemistry on Peroxides and Formaldehyde in Deep Convective Outflow Over the Central and Southeast United States. Journal of Geophysical Research: Atmospheres 123, 7594–7614. https://doi.org/10.1029/2018JD028271

Boeke, N.L., Marshall, J.D., Alvarez, S., Chance, K.V., Fried, A., Kurosu, T.P., Rappenglück, B., Richter, D., Walega, J., Weibring, P., Millet, D.B., 2011. Formaldehyde columns from the Ozone Monitoring Instrument: Urban versus background levels and evaluation using aircraft data and a global model. Journal of Geophysical Research: Atmospheres 116. https://doi.org/10.1029/2010JD014870

Boersma, K.F., Eskes, H.J., Brinksma, E.J., 2004. Error analysis for tropospheric NO2 retrieval from space. Journal of Geophysical Research: Atmospheres 109. https://doi.org/10.1029/2003JD003962

Boersma, K.F., Eskes, H.J., Richter, A., De Smedt, I., Lorente, A., Beirle, S., van Geffen, J.H.G.M., Zara, M., Peters, E., Van Roozendael, M., Wagner, T., Maasakkers, J.D., van der A, R.J., Nightingale, J., De Rudder, A., Irie, H., Pinardi, G., Lambert, J.-C., Compernolle, S.C., 2018. Improving algorithms and uncertainty estimates for satellite NO_2 retrievals: results from the quality assurance for the essential climate variables (QA4ECV) project. Atmospheric Measurement Techniques 11, 6651–6678. https://doi.org/10.5194/amt-11-6651-2018

Boersma, K.F., Eskes, H.J., Veefkind, J.P., Brinksma, E.J., van der A, R.J., Sneep, M., van den Oord, G.H.J., Levelt, P.F., Stammes, P., Gleason, J.F., Bucsela, E.J., 2007. Near-real time retrieval of tropospheric NO_2 from OMI. Atmospheric Chemistry and Physics 7, 2103–2118. https://doi.org/10.5194/acp-7-2103-2007

Box, G.E.P., 1976. Science and Statistics. Journal of the American Statistical Association 71, 791–799. https://doi.org/10.1080/01621459.1976.10480949

Brune, W.H., Miller, D.O., Thames, A.B., Brosius, A.L., Barletta, B., Blake, D.R., Blake, N.J., Chen, G., Choi, Y., Crawford, J.H., Digangi, J.P., Diskin, G., Fried, A., Hall, S.R., Hanisco, T.F., Huey, G.L., Hughes, S.C., Kim, M., Meinardi, S., Montzka, D.D., Pusede, S.E., Schroeder, J.R., Teng, A., Tanner, D.J., Ullmann, K., Walega, J., Weinheimer, A., Wisthaler, A., Wennberg, P.O., 2022. Observations of atmospheric oxidation and ozone production in South Korea. Atmospheric Environment 269, 118854. https://doi.org/10.1016/j.atmosenv.2021.118854

Chan, K.L., Wang, Z., Ding, A., Heue, K.-P., Shen, Y., Wang, J., Zhang, F., Shi, Y., Hao, N., Wenig, M., 2019. MAX-DOAS measurements of tropospheric NO2 and HCHO in Nanjing

935   and a comparison to ozone monitoring instrument observations. Atmospheric Chemistry and
936   Physics 19, 10051–10071. https://doi.org/10.5194/acp-19-10051-2019
937   Chance, K., Palmer, P.I., Spurr, R.J.D., Martin, R.V., Kurosu, T.P., Jacob, D.J., 2000. Satellite
938   observations of formaldehyde over North America from GOME. Geophysical Research
939   Letters 27, 3461–3464. https://doi.org/10.1029/2000GL011857
940   Chance, K., Liu, X., Miller, C.C., Abad, G.G., Huang, G., Nowlan, C., Souri, A., Suleiman, R.,
941   Sun, K., Wang, H., Zhu, L., Zoogman, P., Al-Saadi, J., Antuña-Marrero, J.-C., Carr, J.,
942   Chatfield, R., Chin, M., Cohen, R., Edwards, D., Fishman, J., Flittner, D., Geddes, J.,
943   Grutter, M., Herman, J.R., Jacob, D.J., Janz, S., Joiner, J., Kim, J., Krotkov, N.A., Lefer, B.,
944   Martin, R.V., Mayol-Bracero, O.L., Naeger, A., Newchurch, M., Pfister, G.G., Pickering,
945   K., Pierce, R.B., Cárdenas, C.R., Saiz-Lopez, A., Simpson, W., Spinei, E., Spurr, R.J.D.,
946   Szykman, J.J., Torres, O., Wang, J., 2019. TEMPO Green Paper: Chemistry, physics, and
947   meteorology experiments with the Tropospheric Emissions: monitoring of pollution
948   instrument, in: Sensors, Systems, and Next-Generation Satellites XXIII. Presented at the
949   Sensors, Systems, and Next-Generation Satellites XXIII, SPIE, pp. 56–67.
950   https://doi.org/10.1117/12.2534883
951   Chance, K.V., Burrows, J.P., Perner, D., Schneider, W., 1997. Satellite measurements of
952   atmospheric ozone profiles, including tropospheric ozone, from ultraviolet/visible
953   measurements in the nadir geometry: a potential method to retrieve tropospheric ozone.
954   Journal of Quantitative Spectroscopy and Radiative Transfer 57, 467–476.
955   https://doi.org/10.1016/S0022-4073(96)00157-4
956   Chance, K.V., Burrows, J.P., Schneider, W., 1991. Retrieval and molecule sensitivity studies for
957   the global ozone monitoring experiment and the scanning imaging absorption spectrometer
958   for atmospheric chartography, in: Remote Sensing of Atmospheric Chemistry. Presented at
959   the Remote Sensing of Atmospheric Chemistry, SPIE, pp. 151–165.
960   https://doi.org/10.1117/12.46657
961   Choi, S., Lamsal, L.N., Follette-Cook, M., Joiner, J., Krotkov, N.A., Swartz, W.H., Pickering,
962   K.E., Loughner, C.P., Appel, W., Pfister, G., Saide, P.E., Cohen, R.C., Weinheimer, A.J.,
963   Herman, J.R., 2020. Assessment of NO_2 observations during DISCOVER-AQ and KORUS-
964   AQ field campaigns. Atmospheric Measurement Techniques 13, 2523–2546.
965   https://doi.org/10.5194/amt-13-2523-2020
966   Choi, Y., Kim, H., Tong, D., Lee, P., 2012b. Summertime weekly cycles of observed and
967   modeled NOx and O3 concentrations as a function of satellite-derived ozone production
968   sensitivity and land use types over the Continental United States. Atmospheric Chemistry
969   and Physics 12, 6291–6307. https://doi.org/10.5194/acp-12-6291-2012
970   Choi, Y., Souri, A.H., 2015a. Seasonal behavior and long-term trends of tropospheric ozone, its
971   precursors and chemical conditions over Iran: A view from space. Atmospheric
972   Environment 106, 232–240. https://doi.org/10.1016/j.atmosenv.2015.02.012
973   Choi, Y., Souri, A.H., 2015b. Chemical condition and surface ozone in large cities of Texas
974   during the last decade: Observational evidence from OMI, CAMS, and model analysis.
975   Remote Sensing of Environment 168, 90–101. https://doi.org/10.1016/j.rse.2015.06.026
976   Crawford, J.H., Ahn, J.-Y., Al-Saadi, J., Chang, L., Emmons, L.K., Kim, J., Lee, G., Park, J.-H.,
977   Park, R.J., Woo, J.H., Song, C.-K., Hong, J.-H., Hong, Y.-D., Lefer, B.L., Lee, M., Lee, T.,
978   Kim, S., Min, K.-E., Yum, S.S., Shin, H.J., Kim, Y.-W., Choi, J.-S., Park, J.-S., Szykman,
979   J.J., Long, R.W., Jordan, C.E., Simpson, I.J., Fried, A., Dibb, J.E., Cho, S., Kim, Y.P., 2021.

980   The Korea–United States Air Quality (KORUS-AQ) field study. Elementa: Science of the
981   Anthropocene 9, 00163. https://doi.org/10.1525/elementa.2020.00163
982 de Gouw, J.A., Gilman, J.B., Kim, S.-W., Alvarez, S.L., Dusanter, S., Graus, M., Griffith, S.M.,
983   Isaacman-VanWertz, G., Kuster, W.C., Lefer, B.L., Lerner, B.M., McDonald, B.C.,
984   Rappenglück, B., Roberts, J.M., Stevens, P.S., Stutz, J., Thalman, R., Veres, P.R.,
985   Volkamer, R., Warneke, C., Washenfelder, R.A., Young, C.J., 2018. Chemistry of Volatile
986   Organic Compounds in the Los Angeles Basin: Formation of Oxygenated Compounds and
987   Determination of Emission Ratios. Journal of Geophysical Research: Atmospheres 123,
988   2298–2319. https://doi.org/10.1002/2017JD027976
989 De Smedt, I., Müller, J.-F., Stavrakou, T., van der A, R., Eskes, H., Van Roozendael, M., 2008.
990   Twelve years of global observations of formaldehyde in the troposphere using GOME and
991   SCIAMACHY sensors. Atmospheric Chemistry and Physics 8, 4947–4963.
992   https://doi.org/10.5194/acp-8-4947-2008
993 De Smedt, I., Pinardi, G., Vigouroux, C., Compernolle, S., Bais, A., Benavent, N., Boersma, F.,
994   Chan, K.-L., Donner, S., Eichmann, K.-U., Hedelt, P., Hendrick, F., Irie, H., Kumar, V.,
995   Lambert, J.-C., Langerock, B., Lerot, C., Liu, C., Loyola, D., Piters, A., Richter, A., Rivera
996   Cárdenas, C., Romahn, F., Ryan, R.G., Sinha, V., Theys, N., Vlietinck, J., Wagner, T.,
997   Wang, T., Yu, H., Van Roozendael, M., 2021. Comparative assessment of TROPOMI and
998   OMI formaldehyde observations and validation against MAX-DOAS network column
999   measurements. Atmospheric Chemistry and Physics 21, 12561–12593.
1000   https://doi.org/10.5194/acp-21-12561-2021
1001 De Smedt, I., Stavrakou, T., Hendrick, F., Danckaert, T., Vlemmix, T., Pinardi, G., Theys, N.,
1002   Lerot, C., Gielen, C., Vigouroux, C., Hermans, C., Fayt, C., Veefkind, P., Müller, J.-F., Van
1003   Roozendael, M., 2015. Diurnal, seasonal and long-term variations of global formaldehyde
1004   columns inferred from combined OMI and GOME-2 observations. Atmospheric Chemistry
1005   and Physics 15, 12519–12545. https://doi.org/10.5194/acp-15-12519-2015
1006 De Smedt, I., Stavrakou, T., Müller, J.-F., van der A, R.J., Van Roozendael, M., 2010. Trend
1007   detection in satellite observations of formaldehyde tropospheric columns. Geophysical
1008   Research Letters 37. https://doi.org/10.1029/2010GL044245
1009 De Smedt, I., Theys, N., Yu, H., Danckaert, T., Lerot, C., Compernolle, S., Van Roozendael, M.,
1010   Richter, A., Hilboll, A., Peters, E., Pedergnana, M., Loyola, D., Beirle, S., Wagner, T.,
1011   Eskes, H., van Geffen, J., Boersma, K.F., Veefkind, P., 2018. Algorithm theoretical baseline
1012   for formaldehyde retrievals from S5P TROPOMI and from the QA4ECV project.
1013   Atmospheric Measurement Techniques 11, 2395–2426. https://doi.org/10.5194/amt-11-
1014   2395-2018
1015 Diao, L., Choi, Y., Czader, B., Li, X., Pan, S., Roy, A., Souri, A.H., Estes, M., Jeon, W., 2016.
1016   Discrepancies between modeled and observed nocturnal isoprene in an urban environment
1017   and the possible causes: A case study in Houston. Atmospheric Research 181, 257–264.
1018   https://doi.org/10.1016/j.atmosres.2016.07.009
1019 Duncan, B.N., Yoshida, Y., Olson, J.R., Sillman, S., Martin, R.V., Lamsal, L., Hu, Y., Pickering,
1020   K.E., Retscher, C., Allen, D.J., Crawford, J.H., 2010. Application of OMI observations to a
1021   space-based indicator of NOx and VOC controls on surface ozone formation. Atmospheric
1022   Environment 44, 2213–2223. https://doi.org/10.1016/j.atmosenv.2010.03.010
1023 Fried, A., Walega, J., Weibring, P., Richter, D., Simpson, I.J., Blake, D.R., Blake, N.J., Meinardi,
1024   S., Barletta, B., Hughes, S.C., Crawford, J.H., Diskin, G., Barrick, J., Hair, J., Fenn, M.,
1025   Wisthaler, A., Mikoviny, T., Woo, J.-H., Park, M., Kim, Jinseok, Min, K.-E., Jeong, S.,

Wennberg, P.O., Kim, M.J., Crounse, J.D., Teng, A.P., Bennett, R., Yang-Martin, M., Shook, M.A., Huey, G., Tanner, D., Knote, C., Kim, JongHo, Park, R., Brune, W., 2020. Airborne formaldehyde and volatile organic compound measurements over the Daesan petrochemical complex on Korea's northwest coast during the Korea-United States Air Quality study: Estimation of emission fluxes and effects on air quality. Elementa: Science of the Anthropocene 8, 121. https://doi.org/10.1525/elementa.2020.121

González Abad, G., Liu, X., Chance, K., Wang, H., Kurosu, T.P., Suleiman, R., 2015. Updated Smithsonian Astrophysical Observatory Ozone Monitoring Instrument (SAO OMI) formaldehyde retrieval. Atmospheric Measurement Techniques 8, 19–32. https://doi.org/10.5194/amt-8-19-2015

Gonzalez Abad, G., Souri, A.H., Bak, J., Chance, K., Flynn, L.E., Krotkov, N.A., Lamsal, L., Li, C., Liu, X., Miller, C.C., Nowlan, C.R., Suleiman, R., Wang, H., 2019. Five decades observing Earth's atmospheric trace gases using ultraviolet and visible backscatter solar radiation from space. Journal of Quantitative Spectroscopy and Radiative Transfer 238, 106478. https://doi.org/10.1016/j.jqsrt.2019.04.030

Janjić, T., Bormann, N., Bocquet, M., Carton, J.A., Cohn, S.E., Dance, S.L., Losa, S.N., Nichols, N.K., Potthast, R., Waller, J.A., Weston, P., 2018. On the representation error in data assimilation. Quarterly Journal of the Royal Meteorological Society 144, 1257–1278. https://doi.org/10.1002/qj.3130

Jeon, W., Choi, Y., Souri, A.H., Roy, A., Diao, L., Pan, S., Lee, H.W., Lee, S.-H., 2018. Identification of chemical fingerprints in long-range transport of burning induced upper tropospheric ozone from Colorado to the North Atlantic Ocean. Science of The Total Environment 613–614, 820–828. https://doi.org/10.1016/j.scitotenv.2017.09.177

Jin, X., Fiore, A.M., Murray, L.T., Valin, L.C., Lamsal, L.N., Duncan, B., Folkert Boersma, K., De Smedt, I., Abad, G.G., Chance, K., Tonnesen, G.S., 2017. Evaluating a Space-Based Indicator of Surface Ozone-NOx-VOC Sensitivity Over Midlatitude Source Regions and Application to Decadal Trends. Journal of Geophysical Research: Atmospheres 122, 10,439-10,461. https://doi.org/10.1002/2017JD026720

Jin, X., Holloway, T., 2015. Spatial and temporal variability of ozone sensitivity over China observed from the Ozone Monitoring Instrument. Journal of Geophysical Research: Atmospheres 120, 7229–7246. https://doi.org/10.1002/2015JD023250

Kleinman, L.I., Daum, P.H., Lee, Y.-N., Nunnermacker, L.J., Springston, S.R., Weinstein-Lloyd, J., Rudolph, J., 2001. Sensitivity of ozone production rate to ozone precursors. Geophysical Research Letters 28, 2903–2906. https://doi.org/10.1029/2000GL012597

Laughner, J.L., Zhu, Q., Cohen, R.C., 2019. Evaluation of version 3.0B of the BEHR OMI NO2 product. Atmospheric Measurement Techniques 12, 129–146. https://doi.org/10.5194/amt-12-129-2019

Lee, H.-J., Chang, L.-S., Jaffe, D.A., Bak, J., Liu, X., Abad, G.G., Jo, H.-Y., Jo, Y.-J., Lee, J.-B., Yang, G.-H., Kim, J.-M., Kim, C.-H., 2022. Satellite-Based Diagnosis and Numerical Verification of Ozone Formation Regimes over Nine Megacities in East Asia. Remote Sensing 14, 1285. https://doi.org/10.3390/rs14051285

Lee, Y., Huey, L.G., Wang, Y., Qu, H., Zhang, R., Ji, Y., Tanner, D.J., Wang, X., Tang, J., Song, W., Hu, W., Zhang, Y., 2021. Photochemistry of Volatile Organic Compounds in the Yellow River Delta, China: Formation of O3 and Peroxyacyl Nitrates. Journal of Geophysical Research: Atmospheres 126, e2021JD035296. https://doi.org/10.1029/2021JD035296

Lorente, A., Folkert Boersma, K., Yu, H., Dörner, S., Hilboll, A., Richter, A., Liu, M., Lamsal, L.N., Barkley, M., De Smedt, I., Van Roozendael, M., Wang, Y., Wagner, T., Beirle, S., Lin, J.-T., Krotkov, N., Stammes, P., Wang, P., Eskes, H.J., Krol, M., 2017. Structural uncertainty in air mass factor calculation for NO_2 and HCHO satellite retrievals. Atmospheric Measurement Techniques 10, 759–782. https://doi.org/10.5194/amt-10-759-2017

Martin, R.V., Chance, K., Jacob, D.J., Kurosu, T.P., Spurr, R.J.D., Bucsela, E., Gleason, J.F., Palmer, P.I., Bey, I., Fiore, A.M., Li, Q., Yantosca, R.M., Koelemeijer, R.B.A., 2002. An improved retrieval of tropospheric nitrogen dioxide from GOME. Journal of Geophysical Research: Atmospheres 107, ACH 9-1-ACH 9-21. https://doi.org/10.1029/2001JD001027

Martin, R.V., Fiore, A.M., Van Donkelaar, A., 2004. Space-based diagnosis of surface ozone sensitivity to anthropogenic emissions. Geophysical Research Letters 31. https://doi.org/10.1029/2004GL019416

Matheron, G., 1963. Principles of geostatistics. Economic Geology 58, 1246–1266. https://doi.org/10.2113/gsecongeo.58.8.1246

Miller, D.O., Brune, W.H., 2022. Investigating the Understanding of Oxidation Chemistry Using 20 Years of Airborne OH and HO2 Observations. Journal of Geophysical Research: Atmospheres 127, e2021JD035368. https://doi.org/10.1029/2021JD035368

Newland, M.J., Bryant, D.J., Dunmore, R.E., Bannan, T.J., Acton, W.J.F., Langford, B., Hopkins, J.R., Squires, F.A., Dixon, W., Drysdale, W.S., Ivatt, P.D., Evans, M.J., Edwards, P.M., Whalley, L.K., Heard, D.E., Slater, E.J., Woodward-Massey, R., Ye, C., Mehra, A., Worrall, S.D., Bacak, A., Coe, H., Percival, C.J., Hewitt, C.N., Lee, J.D., Cui, T., Surratt, J.D., Wang, X., Lewis, A.C., Rickard, A.R., Hamilton, J.F., 2021. Low-NO atmospheric oxidation pathways in a polluted megacity. Atmospheric Chemistry and Physics 21, 1613–1625. https://doi.org/10.5194/acp-21-1613-2021

Nowlan, C.R., Liu, X., Janz, S.J., Kowalewski, M.G., Chance, K., Follette-Cook, M.B., Fried, A., González Abad, G., Herman, J.R., Judd, L.M., Kwon, H.-A., Loughner, C.P., Pickering, K.E., Richter, D., Spinei, E., Walega, J., Weibring, P., Weinheimer, A.J., 2018. Nitrogen dioxide and formaldehyde measurements from the GEOstationary Coastal and Air Pollution Events (GEO-CAPE) Airborne Simulator over Houston, Texas. Atmospheric Measurement Techniques 11, 5941–5964. https://doi.org/10.5194/amt-11-5941-2018

Nunnermacker, L.J., Weinstein-Lloyd, J., Kleinman, L., Daum, P.H., Lee, Y.N., Springston, S.R., Klotz, P., Newman, L., Neuroth, G., Hyde, P., 2004. Ground-based and aircraft measurements of trace gases in Phoenix, Arizona (1998). Atmospheric Environment 38, 4941–4956. https://doi.org/10.1016/j.atmosenv.2004.04.033

Pan, S., Choi, Y., Roy, A., Li, X., Jeon, W., Souri, A.H., 2015. Modeling the uncertainty of several VOC and its impact on simulated VOC and ozone in Houston, Texas. Atmospheric Environment 120, 404–416. https://doi.org/10.1016/j.atmosenv.2015.09.029

Rappenglück, B., Ackermann, L., Alvarez, S., Golovko, J., Buhr, M., Field, R.A., Soltis, J., Montague, D.C., Hauze, B., Adamson, S., Risch, D., Wilkerson, G., Bush, D., Stoeckenius, T., Keslar, C., 2014. Strong wintertime ozone events in the Upper Green River basin, Wyoming. Atmospheric Chemistry and Physics 14, 4909–4934. https://doi.org/10.5194/acp-14-4909-2014

Ren, B., Xie, P., Xu, J., Li, A., Qin, M., Hu, R., Zhang, T., Fan, G., Tian, X., Zhu, W., Hu, Z., Huang, Y., Li, X., Meng, F., Zhang, G., Tong, J., Ren, H., Zheng, J., Zhang, Z., Lv, Y., 2022. Vertical characteristics of NO2 and HCHO, and the ozone formation regimes in

1118   Hefei, China. Science of The Total Environment 823, 153425.
1119   https://doi.org/10.1016/j.scitotenv.2022.153425
1120 Schroeder, J.R., Crawford, J.H., Fried, A., Walega, J., Weinheimer, A., Wisthaler, A., Müller,
1121   M., Mikoviny, T., Chen, G., Shook, M., Blake, D.R., Tonnesen, G.S., 2017. New insights
1122   into the column CH2O/NO2 ratio as an indicator of near-surface ozone sensitivity. Journal
1123   of Geophysical Research: Atmospheres 122, 8885–8907.
1124   https://doi.org/10.1002/2017JD026781
1125 Schroeder, J.R., Crawford, J.H., Ahn, J.-Y., Chang, L., Fried, A., Walega, J., Weinheimer, A.,
1126   Montzka, D.D., Hall, S.R., Ullmann, K., Wisthaler, A., Mikoviny, T., Chen, G., Blake,
1127   D.R., Blake, N.J., Hughes, S.C., Meinardi, S., Diskin, G., Digangi, J.P., Choi, Y., Pusede,
1128   S.E., Huey, G.L., Tanner, D.J., Kim, M., Wennberg, P., 2020. Observation-based modeling
1129   of ozone chemistry in the Seoul metropolitan area during the Korea-United States Air
1130   Quality Study (KORUS-AQ). Elementa: Science of the Anthropocene 8, 3.
1131   https://doi.org/10.1525/elementa.400
1132
1133 Schwaerzel, M., Emde, C., Brunner, D., Morales, R., Wagner, T., Berne, A., Buchmann, B.,
1134   Kuhlmann, G., 2020. Three-dimensional radiative transfer effects on airborne and ground-
1135   based trace gas remote sensing. Atmospheric Measurement Techniques 13, 4277–4293.
1136   https://doi.org/10.5194/amt-13-4277-2020
1137 Seinfeld, J. H. and Pandis, S. N., 2006: Atmospheric Chemistry and Physics: From Air Pollution
1138   to Climate Change, 2nd Edn., Wiley-Interscience, Hoboken, N.J., ISBN: 978-1-118-94740-
1139   1.
1140 Sillman, S., He, D., 2002. Some theoretical results concerning O3-NOx-VOC chemistry and
1141   NOx-VOC indicators. Journal of Geophysical Research: Atmospheres 107, ACH 26-1-ACH
1142   26-15. https://doi.org/10.1029/2001JD001123
1143 Sillman, S., Logan, J.A., Wofsy, S.C., 1990. The sensitivity of ozone to nitrogen oxides and
1144   hydrocarbons in regional ozone episodes. Journal of Geophysical Research: Atmospheres
1145   95, 1837–1851. https://doi.org/10.1029/JD095iD02p01837
1146 Souri, A.H., Chance, K., Bak, J., Nowlan, C.R., González Abad, G., Jung, Y., Wong, D.C., Mao,
1147   J., Liu, X., 2021. Unraveling pathways of elevated ozone induced by the 2020 lockdown in
1148   Europe by an observationally constrained regional model using TROPOMI. Atmospheric
1149   Chemistry and Physics 21, 18227–18245. https://doi.org/10.5194/acp-21-18227-2021
1150 Souri, A.H., Chance, K., Sun, K., Liu, X., Johnson, M.S., 2022. Dealing with spatial
1151   heterogeneity in pointwise-to-gridded- data comparisons. Atmospheric Measurement
1152   Techniques 15, 41–59. https://doi.org/10.5194/amt-15-41-2022
1153 Souri, A.H., Nowlan, C.R., Wolfe, G.M., Lamsal, L.N., Chan Miller, C.E., Abad, G.G., Janz,
1154   S.J., Fried, A., Blake, D.R., Weinheimer, A.J., Diskin, G.S., Liu, X., Chance, K., 2020.
1155   Revisiting the effectiveness of HCHO/NO2 ratios for inferring ozone sensitivity to its
1156   precursors using high resolution airborne remote sensing observations in a high ozone
1157   episode during the KORUS-AQ campaign. Atmospheric Environment 224, 117341.
1158   https://doi.org/10.1016/j.atmosenv.2020.117341
1159   Souri. (2022). ahsouri/STREET: STREET 0.0.2 (0.0.2). Zenodo.
1160   https://doi.org/10.5281/zenodo.6993116
1161 Tang, W., Edwards, D.P., Emmons, L.K., Worden, H.M., Judd, L.M., Lamsal, L.N., Al-Saadi,
1162   J.A., Janz, S.J., Crawford, J.H., Deeter, M.N., Pfister, G., Buchholz, R.R., Gaubert, B.,
1163   Nowlan, C.R., 2021. Assessing sub-grid variability within satellite pixels over urban regions

using airborne mapping spectrometer measurements. Atmospheric Measurement Techniques 14, 4639–4655. https://doi.org/10.5194/amt-14-4639-2021

Thornton, J.A., Wooldridge, P.J., Cohen, R.C., Martinez, M., Harder, H., Brune, W.H., Williams, E.J., Roberts, J.M., Fehsenfeld, F.C., Hall, S.R., Shetter, R.E., Wert, B.P., Fried, A., 2002. Ozone production rates as a function of NOx abundances and HOx production rates in the Nashville urban plume. Journal of Geophysical Research: Atmospheres 107, ACH 7-1-ACH 7-17. https://doi.org/10.1029/2001JD000932

Tonnesen, G.S., Dennis, R.L., 2000a. Analysis of radical propagation efficiency to assess ozone sensitivity to hydrocarbons and NO x : 1. Local indicators of instantaneous odd oxygen production sensitivity. Journal of Geophysical Research: Atmospheres 105, 9213–9225. https://doi.org/10.1029/1999JD900371

Tonnesen, G.S., Dennis, R.L., 2000b. Analysis of radical propagation efficiency to assess ozone sensitivity to hydrocarbons and NO x : 2. Long-lived species as indicators of ozone concentration sensitivity. Journal of Geophysical Research: Atmospheres 105, 9227–9241. https://doi.org/10.1029/1999JD900372

Valin, L.C., Russell, A.R., Hudman, R.C., Cohen, R.C., 2011. Effects of model resolution on the interpretation of satellite NO2 observations. Atmospheric Chemistry and Physics 11, 11647–11655. https://doi.org/10.5194/acp-11-11647-2011

van Geffen, J., Eskes, H., Compernolle, S., Pinardi, G., Verhoelst, T., Lambert, J.-C., Sneep, M., ter Linden, M., Ludewig, A., Boersma, K.F., Veefkind, J.P., 2022. Sentinel-5P TROPOMI NO₂ retrieval: impact of version v2.2 improvements and comparisons with OMI and ground-based data. Atmospheric Measurement Techniques 15, 2037–2060. https://doi.org/10.5194/amt-15-2037-2022

Verhoelst, T., Compernolle, S., Pinardi, G., Lambert, J.-C., Eskes, H.J., Eichmann, K.-U., Fjæraa, A.M., Granville, J., Niemeijer, S., Cede, A., Tiefengraber, M., Hendrick, F., Pazmiño, A., Bais, A., Bazureau, A., Boersma, K.F., Bognar, K., Dehn, A., Donner, S., Elokhov, A., Gebetsberger, M., Goutail, F., Grutter de la Mora, M., Gruzdev, A., Gratsea, M., Hansen, G.H., Irie, H., Jepsen, N., Kanaya, Y., Karagkiozidis, D., Kivi, R., Kreher, K., Levelt, P.F., Liu, C., Müller, M., Navarro Comas, M., Piters, A.J.M., Pommereau, J.-P., Portafaix, T., Prados-Roman, C., Puentedura, O., Querel, R., Remmers, J., Richter, A., Rimmer, J., Rivera Cárdenas, C., Saavedra de Miguel, L., Sinyakov, V.P., Stremme, W., Strong, K., Van Roozendael, M., Veefkind, J.P., Wagner, T., Wittrock, F., Yela González, M., Zehner, C., 2021. Ground-based validation of the Copernicus Sentinel-5P TROPOMI NO₂ measurements with the NDACC ZSL-DOAS, MAX-DOAS and Pandonia global networks. Atmospheric Measurement Techniques 14, 481–510. https://doi.org/10.5194/amt-14-481-2021

Vigouroux, C., Langerock, B., Bauer Aquino, C. A., Blumenstock, T., Cheng, Z., De Mazière, M., De Smedt, I., Grutter, M., Hannigan, J. W., Jones, N., Kivi, R., Loyola, D., Lutsch, E., Mahieu, E., Makarova, M., Metzger, J.-M., Morino, I., Murata, I., Nagahama, T., Notholt, J., Ortega, I., Palm, M., Pinardi, G., Röhling, A., Smale, D., Stremme, W., Strong, K., Sussmann, R., Té, Y., van Roozendael, M., Wang, P., and Winkler, H.: TROPOMI–Sentinel-5 Precursor formaldehyde validation using an extensive network of ground-based Fourier-transform infrared stations, Atmos. Meas. Tech., 13, 3751–3767, https://doi.org/10.5194/amt-13-3751-2020, 2020.

Wells, K.C., Millet, D.B., Payne, V.H., Deventer, M.J., Bates, K.H., de Gouw, J.A., Graus, M., Warneke, C., Wisthaler, A., Fuentes, J.D., 2020. Satellite isoprene retrievals constrain

1210   emissions and atmospheric oxidation. Nature 585, 225–233. https://doi.org/10.1038/s41586-
1211   020-2664-3

1212 Wolfe, G. M., Kaiser, J., Hanisco, T.F., Keutsch, F.N., de Gouw, J.A., Gilman, J.B., Graus, M.,
1213   Hatch, C.D., Holloway, J., Horowitz, L.W., Lee, B.H., Lerner, B.M., Lopez-Hilifiker, F.,
1214   Mao, J., Marvin, M.R., Peischl, J., Pollack, I.B., Roberts, J.M., Ryerson, T.B., Thornton,
1215   J.A., Veres, P.R., Warneke, C., 2016. Formaldehyde production from isoprene oxidation
1216   across NO_x regimes. Atmospheric Chemistry and Physics 16, 2597–2610.
1217   https://doi.org/10.5194/acp-16-2597-2016

1218 Wolfe, Glenn M., Marvin, M.R., Roberts, S.J., Travis, K.R., Liao, J., 2016. The Framework for
1219   0-D Atmospheric Modeling (F0AM) v3.1. Geoscientific Model Development 9, 3309–3319.
1220   https://doi.org/10.5194/gmd-9-3309-2016

1221 Xu, W., Zhang, G., Wang, Y., Tong, S., Zhang, W., Ma, Z., Lin, W., Kuang, Y., Yin, L., Xu, X.,
1222   2021. Aerosol Promotes Peroxyacetyl Nitrate Formation During Winter in the North China
1223   Plain. Environ. Sci. Technol. 55, 3568–3581. https://doi.org/10.1021/acs.est.0c08157

1224 Yang, K., Carn, S.A., Ge, C., Wang, J., Dickerson, R.R., 2014. Advancing measurements of
1225   tropospheric NO2 from space: New algorithm and first global results from OMPS.
1226   Geophysical Research Letters 41, 4777–4786. https://doi.org/10.1002/2014GL060136

1227 Zhang, K., Duan, Y., Huo, J., Huang, L., Wang, Yangjun, Fu, Q., Wang, Yuhang, Li, L., 2021.
1228   Formation mechanism of HCHO pollution in the suburban Yangtze River Delta region,
1229   China: A box model study and policy implementations. Atmospheric Environment 267,
1230   118755. https://doi.org/10.1016/j.atmosenv.2021.118755

1231 Zhu, L., González Abad, G., Nowlan, C.R., Chan Miller, C., Chance, K., Apel, E.C., DiGangi,
1232   J.P., Fried, A., Hanisco, T.F., Hornbrook, R.S., Hu, L., Kaiser, J., Keutsch, F.N., Permar,
1233   W., St. Clair, J.M., Wolfe, G.M., 2020. Validation of satellite formaldehyde (HCHO)
1234   retrievals using observations from 12 aircraft campaigns. Atmospheric Chemistry and
1235   Physics 20, 12329–12345. https://doi.org/10.5194/acp-20-12329-2020

1236 Zhu, L., Jacob, D.J., Kim, P.S., Fisher, J.A., Yu, K., Travis, K.R., Mickley, L.J., Yantosca, R.M.,
1237   Sulprizio, M.P., De Smedt, I., González Abad, G., Chance, K., Li, C., Ferrare, R., Fried, A.,
1238   Hair, J.W., Hanisco, T.F., Richter, D., Jo Scarino, A., Walega, J., Weibring, P., Wolfe,
1239   G.M., 2016. Observing atmospheric formaldehyde (HCHO) from space: validation and
1240   intercomparison of six retrievals from four satellites (OMI, GOME2A, GOME2B, OMPS)
1241   with SEAC[4]RS aircraft observations over the southeast US. Atmospheric Chemistry and
1242   Physics 16, 13477–13490. https://doi.org/10.5194/acp-16-13477-2016

1243 Zhu, L., Jacob, D.J., Mickley, L.J., Marais, E.A., Cohan, D.S., Yoshida, Y., Duncan, B.N., Abad,
1244   G.G., Chance, K.V., 2014. Anthropogenic emissions of highly reactive volatile organic
1245   compounds in eastern Texas inferred from oversampling of satellite (OMI) measurements of
1246   HCHO columns. Environ. Res. Lett. 9, 114004. https://doi.org/10.1088/1748-
1247   9326/9/11/114004

1248

1249
1250
1251   **Table1.** The box model configurations and inputs.

Temporal resolution of samples	10-15 sec
Time steps	1 hour
Number of solar cycles	5
Dilution constant	$1/86400 - 1/43200\ (s^{-1})$
Meteorological Inputs	Pressure, Temperature, and Relative Humidity
Photolysis frequencies estimates	LUT based on the NCAR TUV model calculations
Photolysis frequencies constraints (campaign#‡)	Measured jNO_2 (1-4) and jO^1D (4)
Compounds (Instrument#†, campaign#‡) used for constraining the box model	H_2(1, 4)§, CO (4, 1-4), NO_x (2, 1-4), O_3 (2, 1-4), SO_2 (6, 4) , CH_4 (4, 1-4), HNO_3 (10, 1-4), Isoprene (9, 1-4), Monoterpenes (9, 1-4), Acetone (9, 1-4), Ethylene (1, 4), Ethane (1, 4), Methanol (9, 1-4), Propane (1, 4), Benzene (1 or 9, 2-4), Xylene (1 or 9, 1 and 4), Toluene (1 or 9, 1-4), Glyoxal (8, 4), Acetaldehyde (9, 1-4), Methyl vinyl ketone (9, 1-4), Methyl Ethyl Ketone (9, 2-4), Propene (1 or 9, 2 and 4), Acetic acid (9, 2-4), Glycolaldehyde (5, 4), H_2O_2 (5, 4)
Unconstrained compounds (Instrument#†, campaign#‡) used for validation	HO_2 (3, 4), OH (3, 4), NO (2, 1-4), NO_2 (2, 1-4), PAN (10, 1-4), HCHO (7, 1-4)
Chemical Mechanism	CB06

1252
1253   † (1) UC Irvine's Whole Air Sampler (WAS), (2) NCAR 4-Channel Chemiluminescence, (3) Penn
1254   State's Airborne Tropospheric Hydrogen Oxides Sensor (ATHOS), (4) NASA Langley's DACOM
1255   tunable diode laser spectrometer, (5) Caltech's single mass analyzer, (6) Georgia Tech's ionization
1256   mass spectrometer, (7) The University of Colorado at Boulder's the Compact Atmospheric Multi-
1257   species Spectrometer (CAMS), (8) Korean Airborne Cavity Enhances Spectrometer, (9)
1258   University of Innsbruck's PTR-TOF-MS instrument, and (10) University of California, Berkeley's
1259   TD-LIF.
1260
1261   ‡ (1) DISCOVER-Baltimore-Washington, (2) DISCOVER-Texas-Houston, (3) DISCOVER-
1262   Colorado, and (4) KORUS-AQ
1263
1264   § In the absence of measurements, a default value of 550 ppbv is specified.
1265

1266
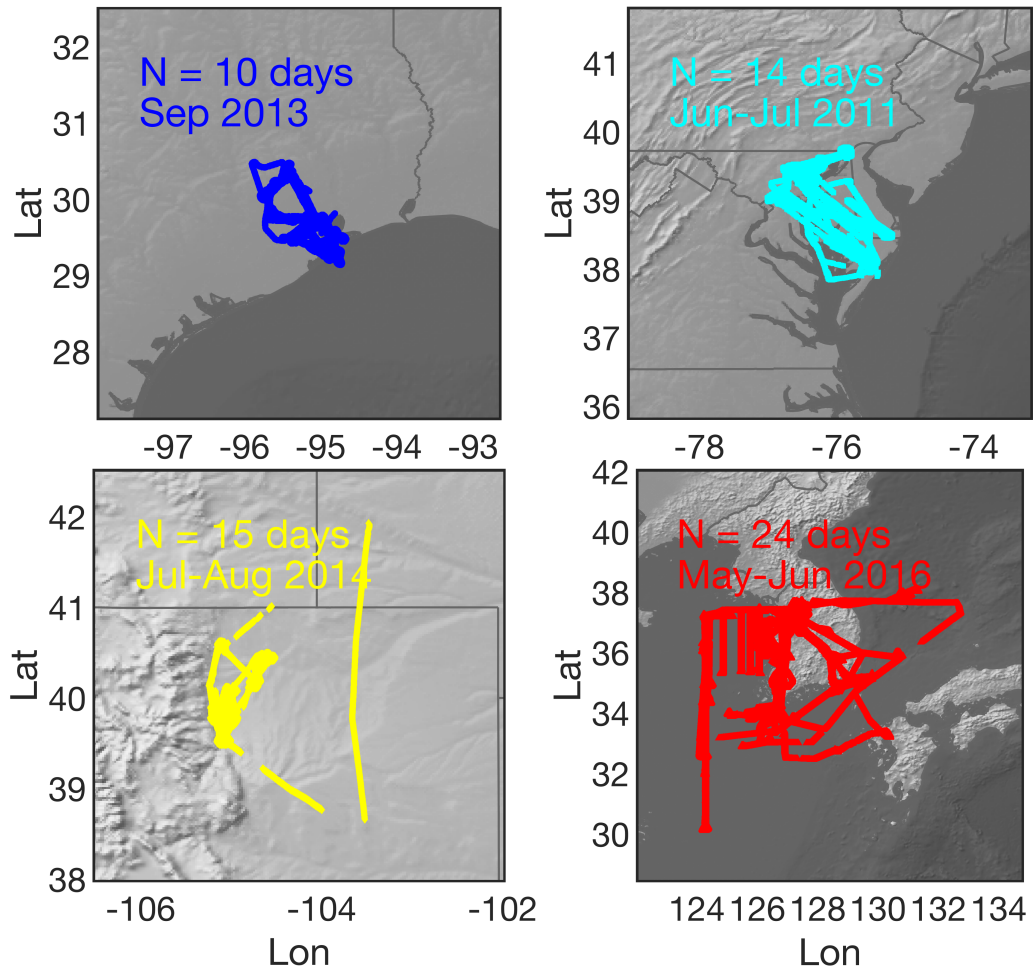
1267
1268
1269 **Figure 1.** The spatial distributions of aircraft measurements collected during NASA's a)
1270 DISCOVER-AQ Houston-Texas, b) DISCOVER-AQ Baltimore-Washington, c) DISCOVER-AQ
1271 Colorado, and d) KORUS-AQ. The duration of each campaign is based on how long the aircraft
1272 was in the air.
1273
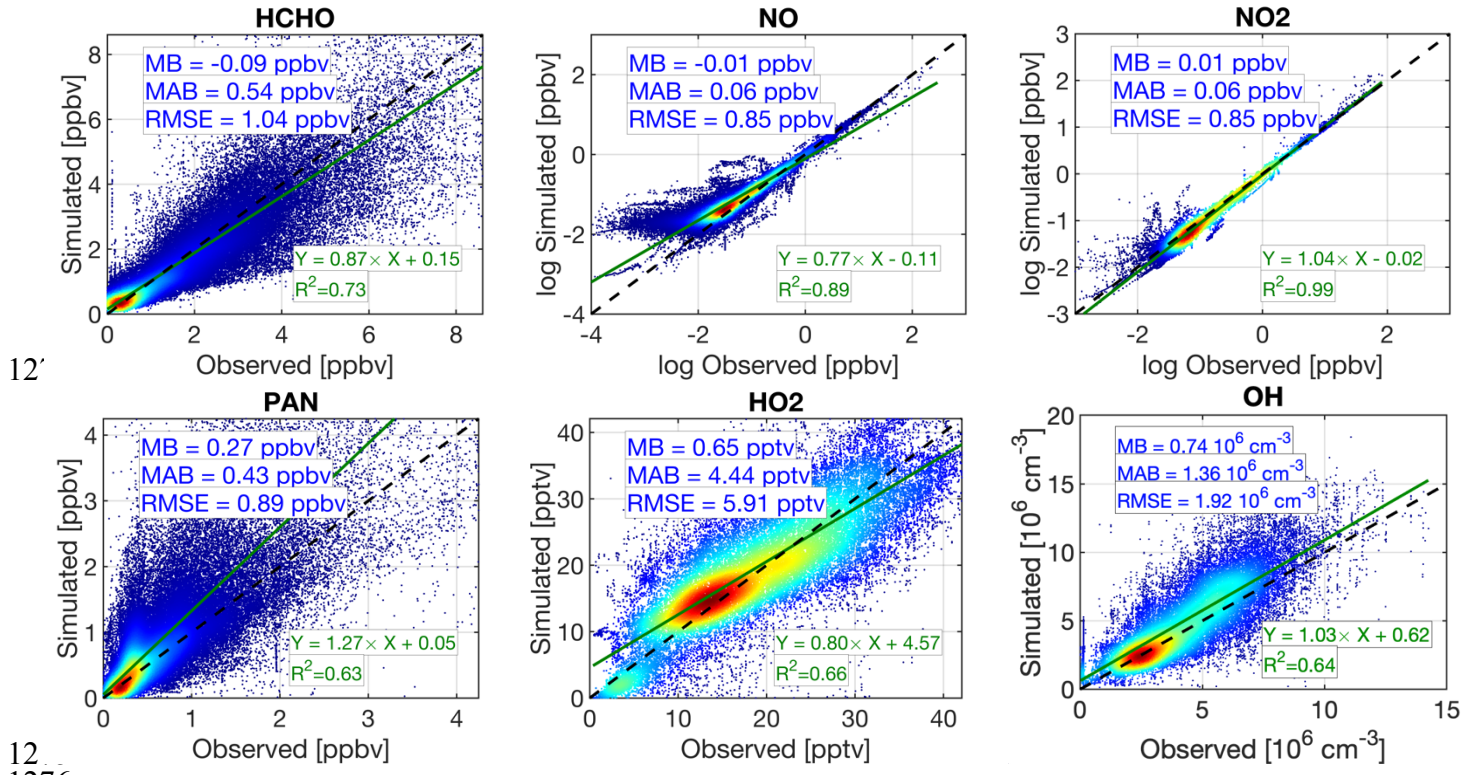
Figure 2. The comparisons of the observed concentrations of several critical compounds to those simulated by our F0AM box model. Each subplot contains mean bias (MB), mean absolute bias (MAB), and root mean square error (RMSE). The least-squares fit to the paired data, along with the coefficient of determination (R^2) are also individually shown for each compound. Note that we do not account for the observations errors in the x-axis. The concentrations of NO and NO_2 are log-transformed.
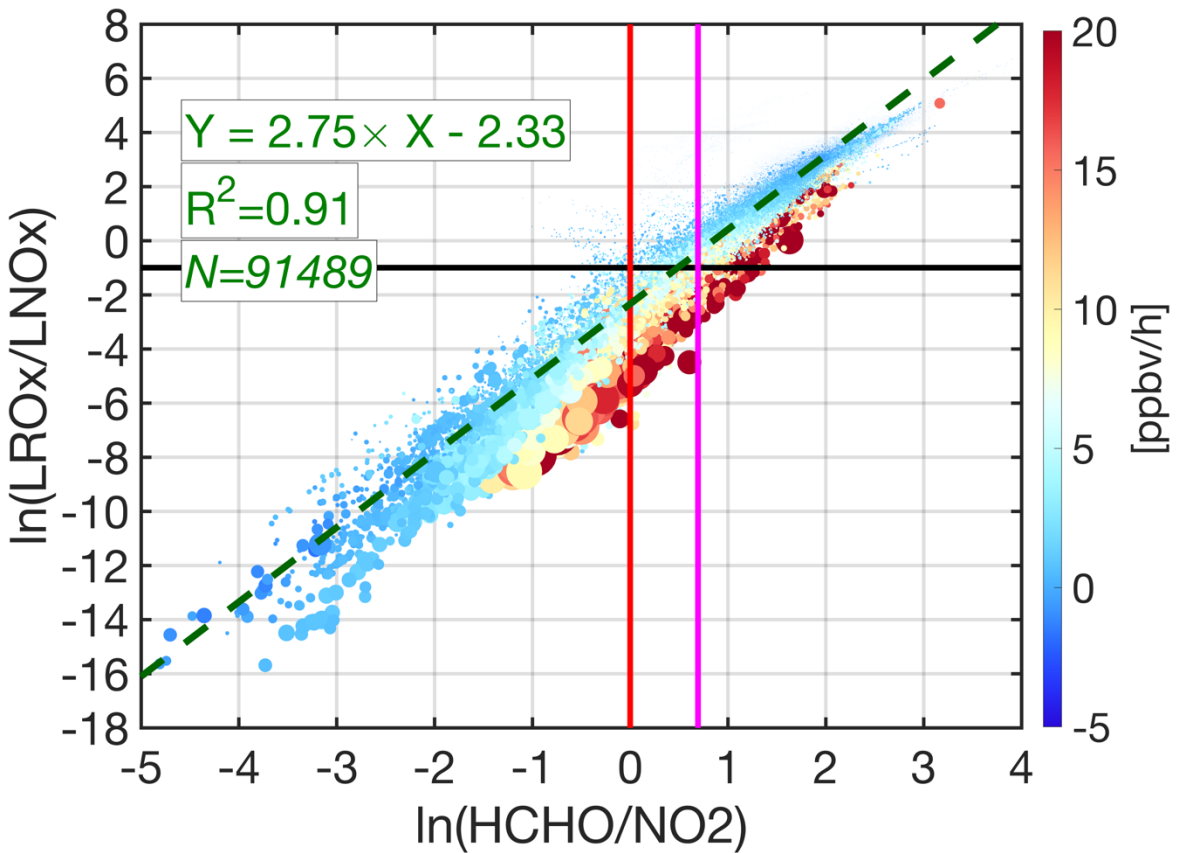
Figure 3. The scatterplot of natural logarithm-transformed of $HCHO/NO_2$ versus LROx/LNOx based on the simulated values performed by the F0AM box model. The heat color indicates the calculated ozone production rates (PO_3). The size of each data point is proportional to $HCHO \times NO_2$. The black line is the baseline separator of NOx-sensitive (above the line) and VOC-sensitive (below the line) regimes. We overlay $HCHO/NO_2 = 1$ and $HCHO/NO_2 = 2$ as red and purple lines, respectively. The dashed dark green line indicates the least-squares fit to the paired data. The $HCHO/NO_2 = 1.8$ with a 20% error is the optimal transitioning point based on this result.
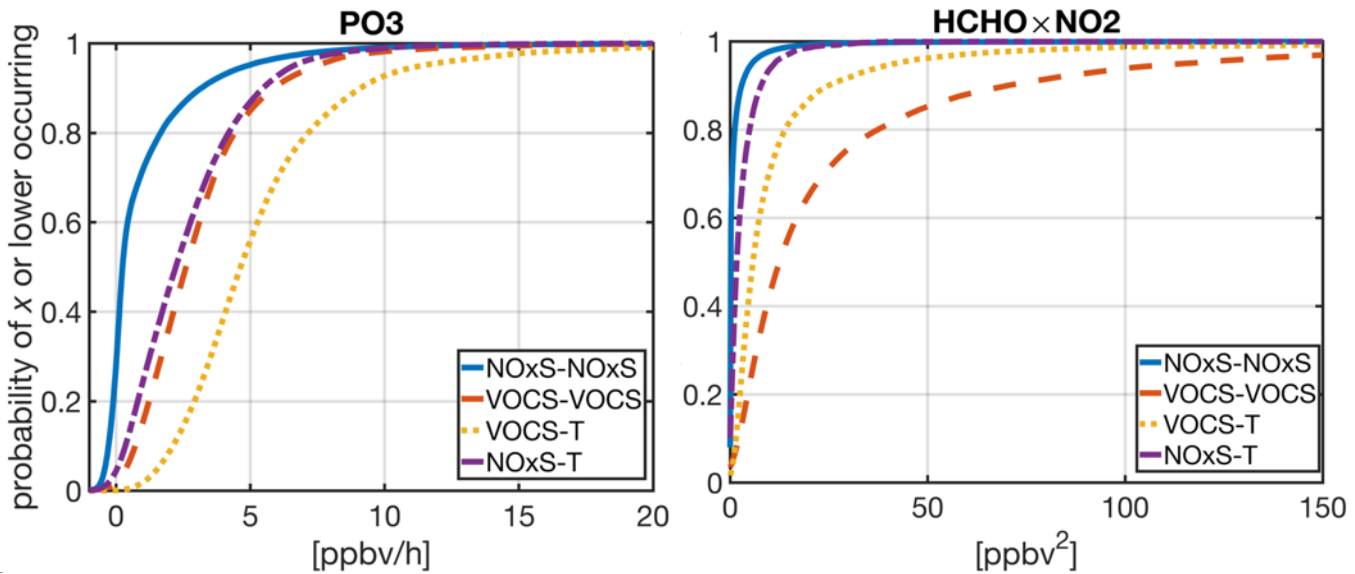
Figure 4. Cumulative distribution functions of PO_3 and $HCHO \times NO_2$ simulated by the box model constrained by NASA's aircraft observations. Four regions are shown: NOx-sensitive — NOx-sensitive, NOx-sensitive—transitional, VOC-sensitive—transitional, and VOC-sensitive—VOC-sensitive. The first name of the regime is based on the baseline ($\ln(LROx/LNOx)=-1.0$), whereas the second one follows those defined in Duncan et al. (2010): VOC-sensitive if $HCHO/NO_2<1$, transitional if $1<HCHO/NO_2<2$, and NO_x-sensitive if $HCHO/NO_2>2$.
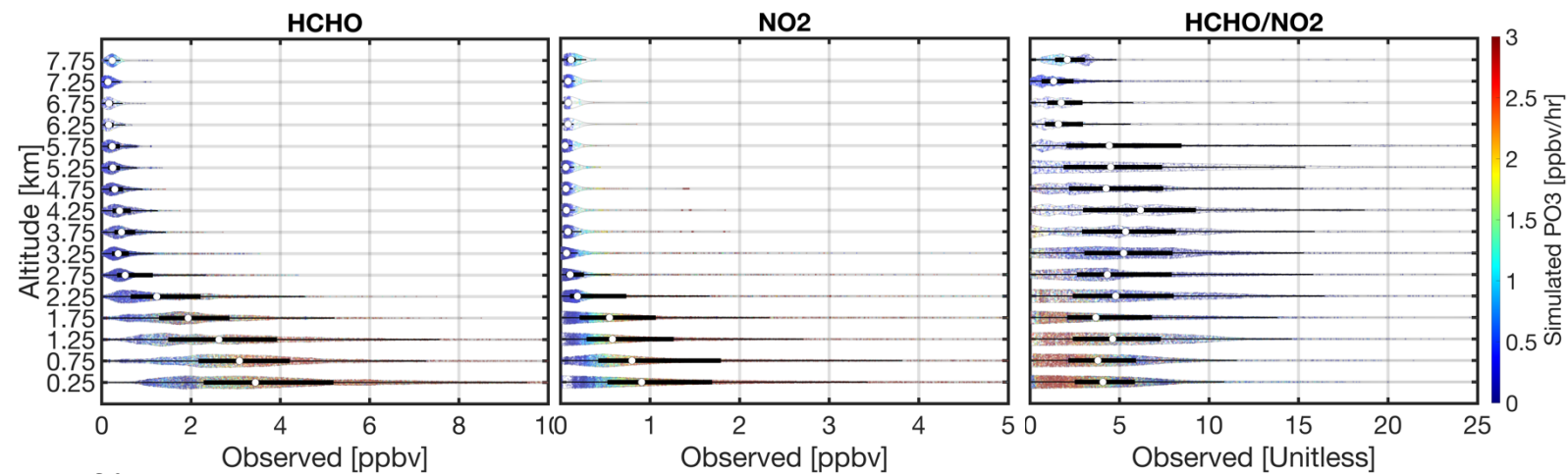
Figure 5. The violin plots of the afternoon vertical distribution of HCHO, NO_2, and $HCHO/NO_2$ observations collected during DISCOVER-AQ Texas, Colorado, Maryland, and KORUS-AQ campaigns. The violin plots demonstrate the distribution of data (i.e., a wider width means a higher frequency). White dots show the median. A solid black line shows both the 25th and 75th percentiles. The heatmap denotes the simulated ozone production rates.
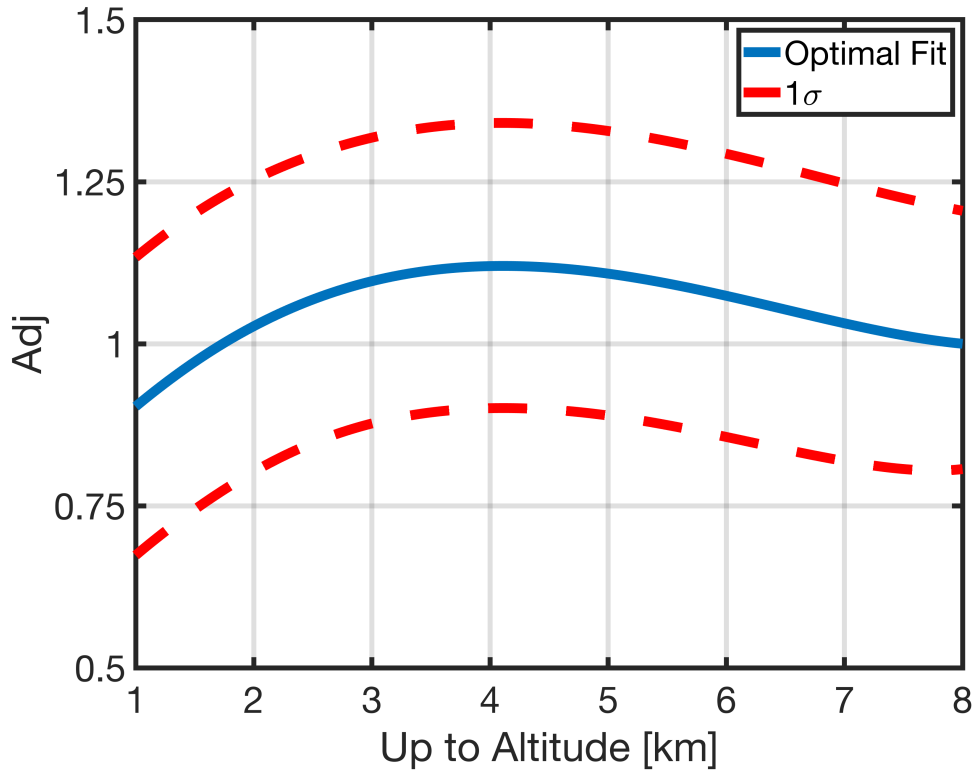
1308
1309
1310 **Figure 6.** The adjustment factor is the ratio of the centroid of the polygon bounding 25th and 75th
1311 percentiles of the observed HCHO/NO$_2$ columns by NASA's aircraft between the surface to 8 km
1312 to the ones between the surface and the desired altitude. This factor can be easily applied to the
1313 observed HCHO/NO$_2$ columns to translate the value to the desired altitude stretching down to the
1314 surface (i.e., PBLH). The optimal curve follows a quadratic function formulated in Eq.11.
1315
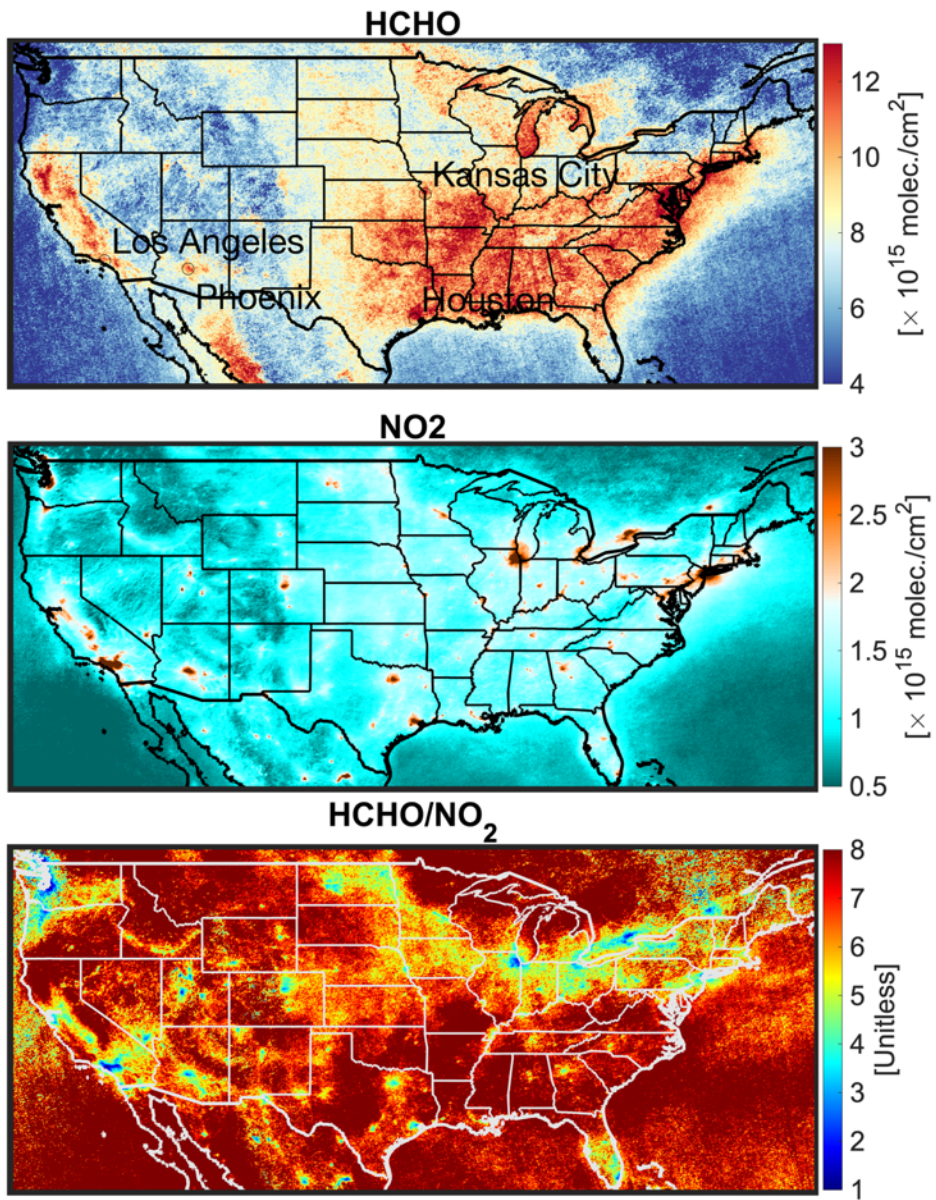
Figure 7. Oversampled TROPOMI total HCHO columns (top), tropospheric NO₂ columns (middle), and the ratio (bottom) at 3×3 km² from June till August 2021 over the US. The ratio map is derived from the averaged maps shown in the top and middle panels.
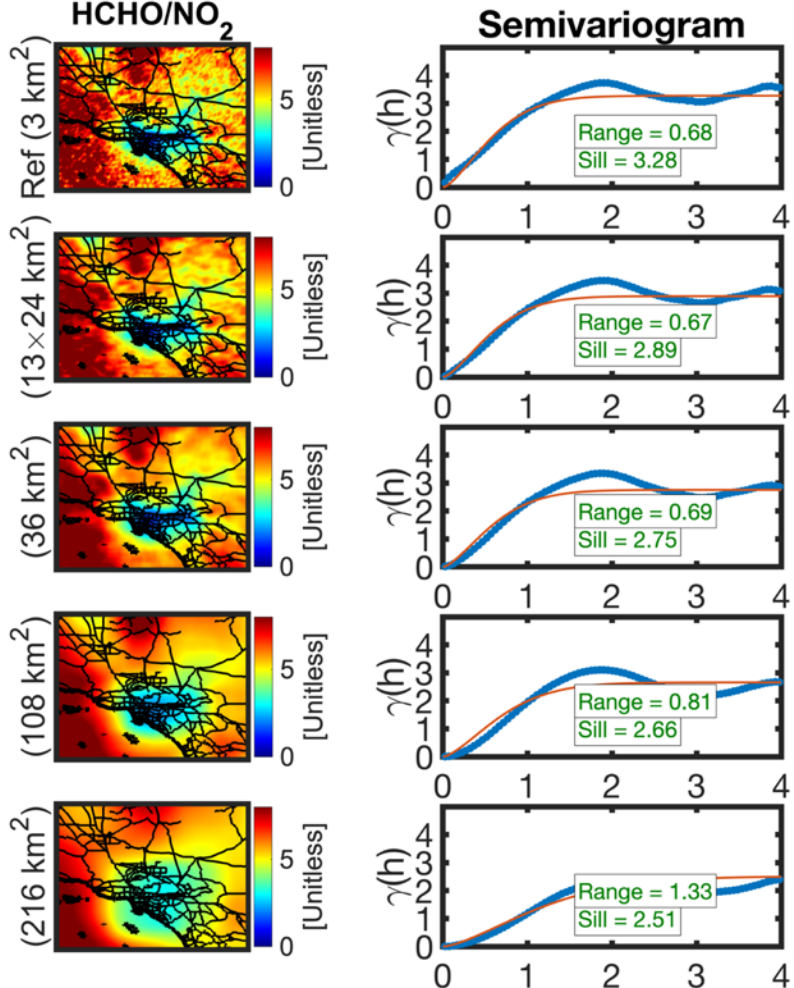
1321
Figure 8. The first column represents the spatial map of HCHO/NO₂ ratios over Los Angeles from June till August 2021 at different spatial resolutions. To upscale each map to a coarser footprint, we use an ideal box filter tailored to the target resolution. The second column shows the semivariograms corresponding to the left map along with the fitted curve (red line). The sill and the range are computed based on the fitted curve. The x-axis in the semivariogram is in degrees (1 degree ~ 110 km).
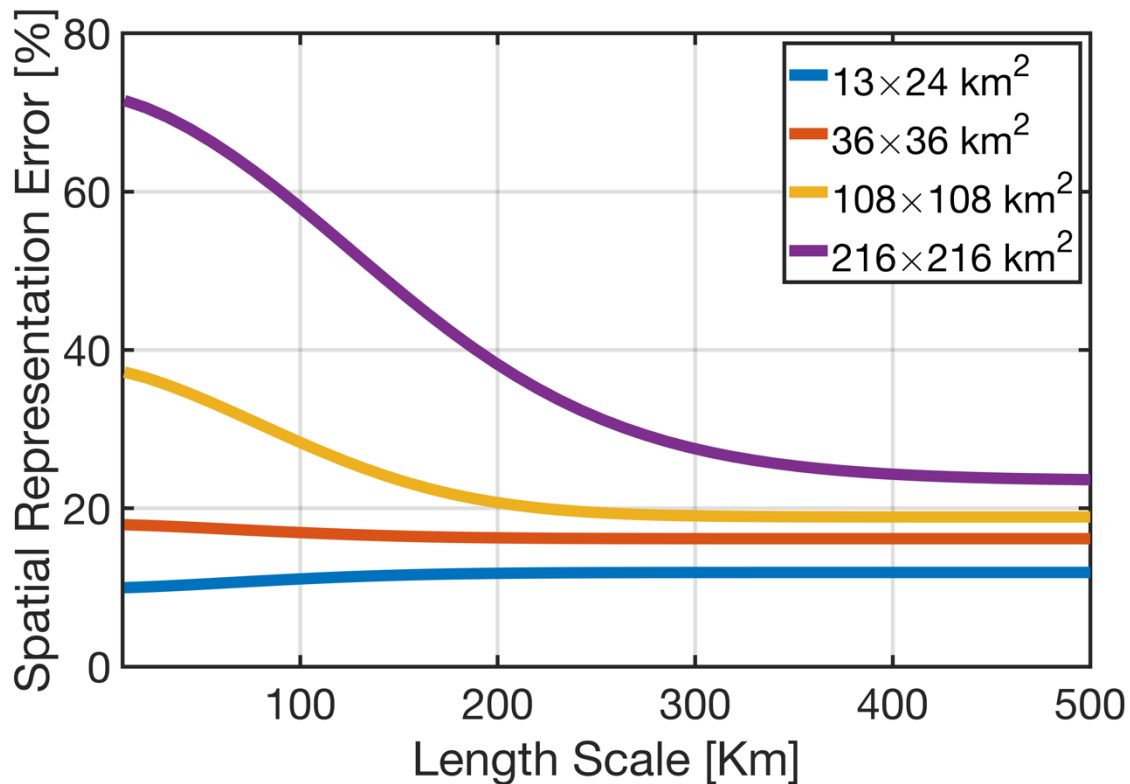
**Figure 9.** The spatial representation errors quantified based on the proposed method in this study. The error explains the spatial loss (or variance) due to the footprint of a hypothetical sensor at different length scales. To put this error in perspective, a grid box with 216×216 km^2 will naturally lose 65% of the spatial variance existing in the ratio at the scale of Los Angeles, which is roughly 50 km wide. All of these numbers are in reference to the TROPOMI 3×3 km^2.

TROPOMI (Δ Trop NO2)

σ=3.56
μ=-1.85
Median=-0.98
Skewness=-4.63
N=3402
R^2 (fit)=0.95
σ (fit)=2.12

OMI (Δ Trop NO2)

σ=6.57
μ=-3.24
Median=-1.94
Skewness=-5.19
N=217
R^2 (fit)=0.96
σ (fit)=2.37

$[\times 10^{15}$ molec./cm$^2]$
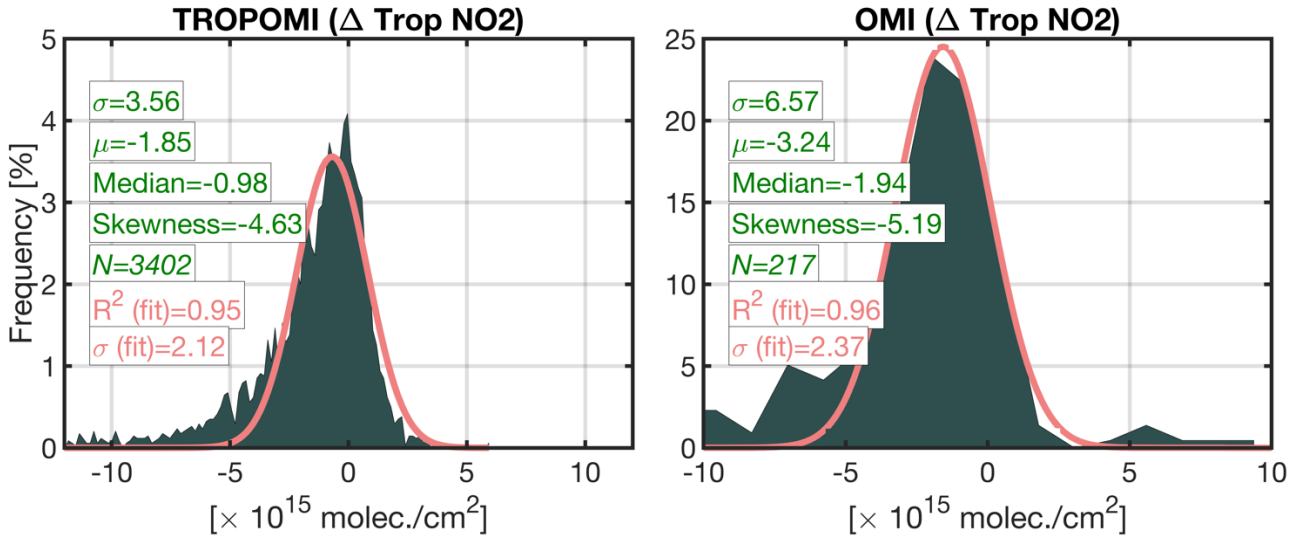
Figure 10. The histogram of the differences between TROPOMI and OMI and benchmarks. MAX-DOAS and integrated aircraft spirals are the TROPOMI and the OMI benchmarks, respectively. The data curation and relevant criteria on how they have been paired can be found in Verholest et al. (2021) and Choi et al. (2020). The statistics in green are based on all data, whereas those in pink are based on the fitted Gaussian function.
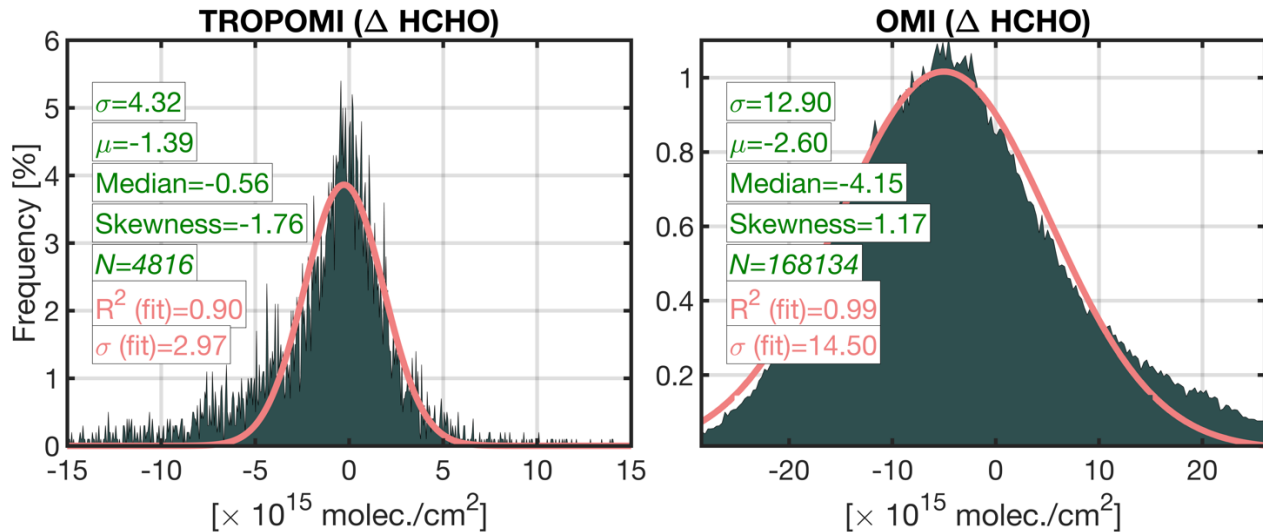
**Figure 11.** The histogram of the differences between TROPOMI and OMI and benchmarks. FTIR and corrected GEOS-Chem simulations are the TROPOMI and the OMI benchmarks. The data curation and relevant criteria on how they have been paired can be found in Vigouroux et al. (2021) and Zhu et al. (2020). The statistics in green color are based on all data, whereas those in pink are based on the fitted Gaussian function.
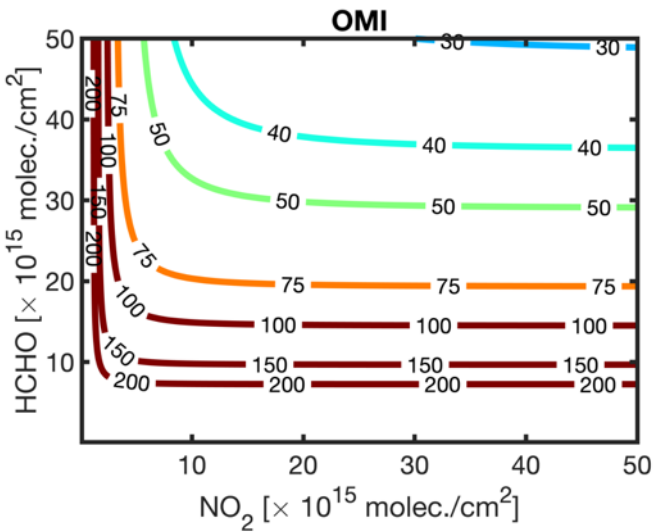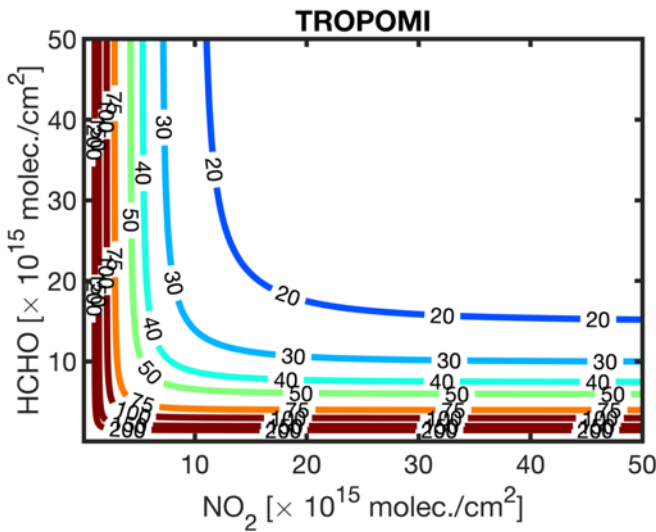
**Figure 12.** The contour plots of the relative errors in TROPOMI (left) and OMI (right) based on dispersions derived from Figures 10 and 11. The errors used for these estimates are based on daily observations.
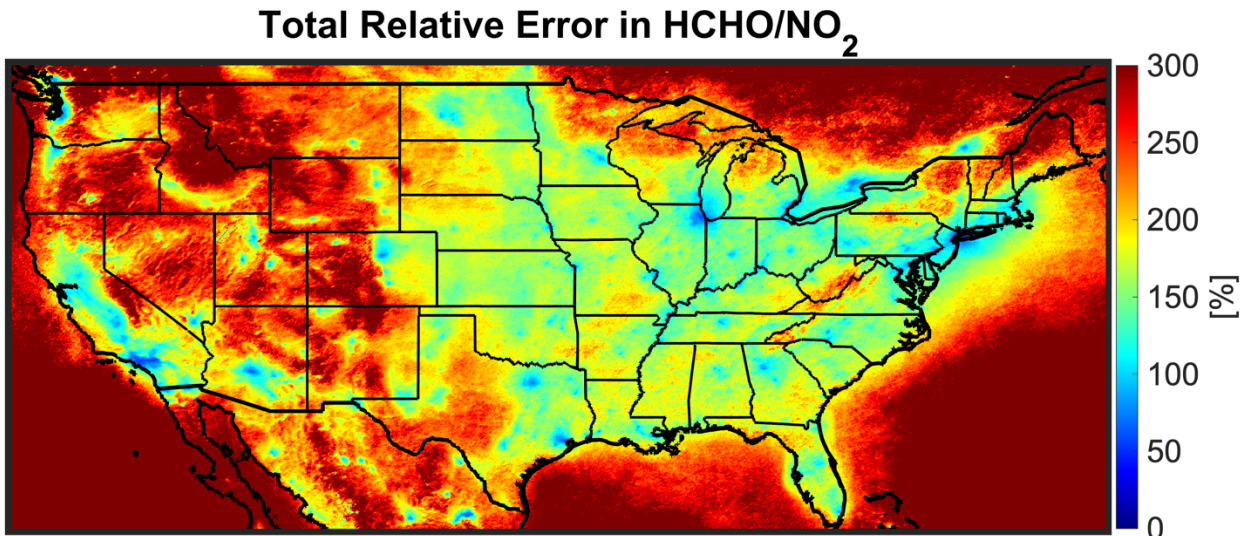
Total Relative Error in HCHO/NO$_2$

Figure 13. The total relative error for observed TROPOMI HCHO/NO$_2$ ratios considering the daily TROPOMI retrieval errors (σ_{NO_2}= 2.11×10^{15} molec./cm^2 and σ_{HCHO}= 2.97×10^{15} molec./cm^2), the spatial representation pertaining to OMI footprint over a city environment (13% loss in the spatial variance), and the column to the PBL translation parameterization (26%) proposed in this study. Please note that the observed FNR is based on mean values from June to August 2021, while the uncertainties used for error calculation are on a daily-basis.

HCHO = 8×10^15 , NO2 = 1×10^16 , OMI (13x24 km²)

Retrieval
Column-to-PBL
Spatial Representation

37%
52%
10%

HCHO = 8×10^15 , NO2 = 1×10^16 , 108 km²

29%
6%
65%

HCHO = 3×10^15 , NO2 = 5×10^15 , OMI (13x24 km²)

10%
3%
87%

HCHO = 3×10^15 , NO2 = 5×10^15 , 108 km²

25%
2%
73%
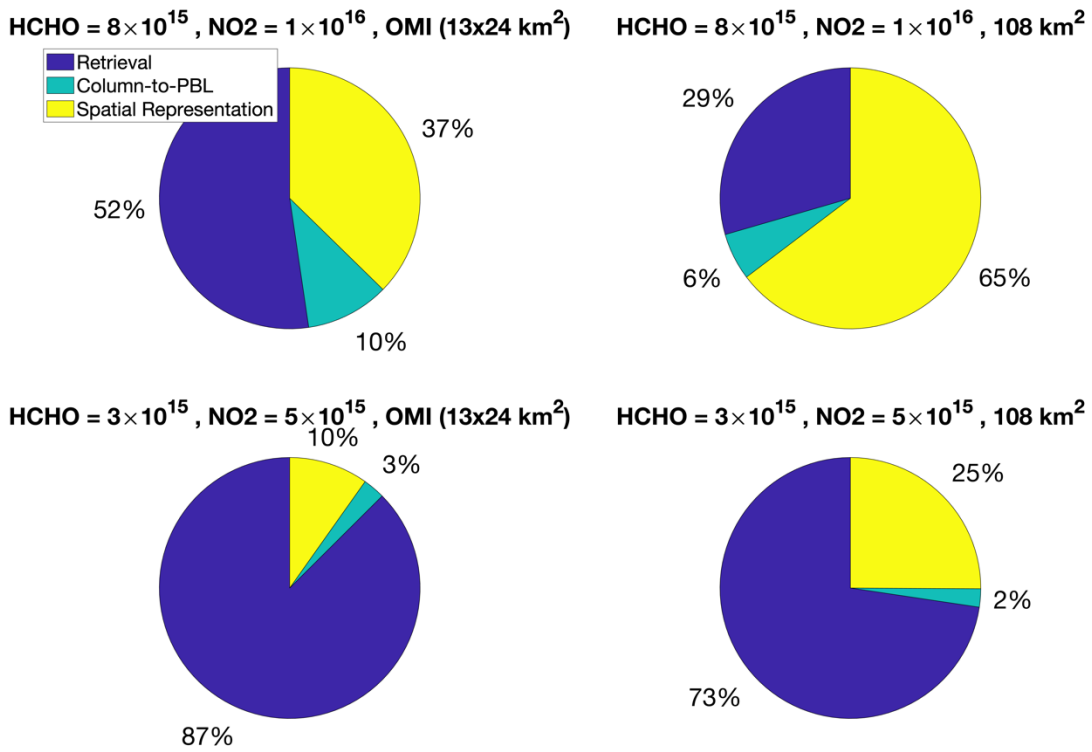
1365

1366 **Figure 14.** The fractional errors of retrieval (blue), column to PBL translation (green), and spatial
1367 representation (yellow) of the total error budget for different concentrations and footprints based
1368 on TROPOMI sigma values. The retrieval error used for the error budget is on a daily basis.
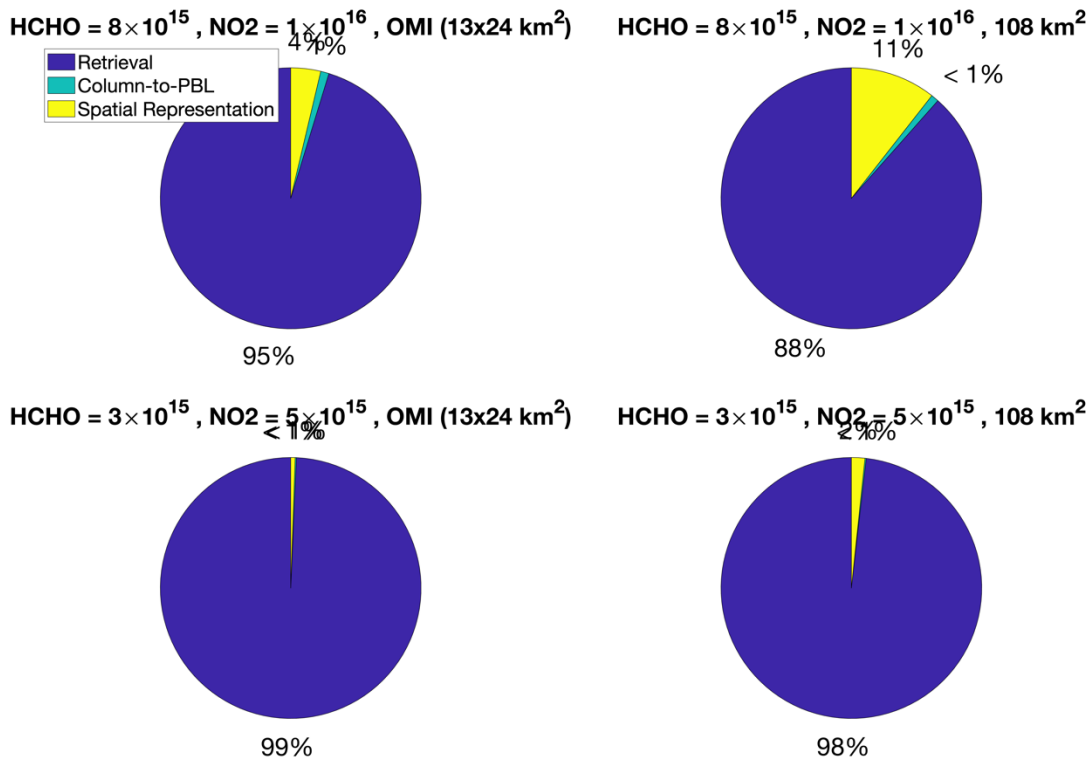
Figure 15. Same as Figure 14 but based on OMI sigma values.